Journal Pre-proof

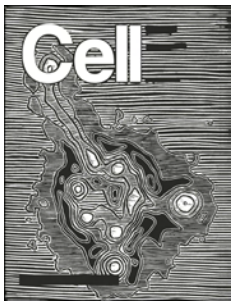

SARS-CoV-2 Reverse Genetics Reveals a Variable Infection Gradient in the Respiratory Tract

Yixuan J. Hou, Kenichi Okuda, Caitlin E. Edwards, David R. Martinez, Takanori Asakura, Kenneth H. Dinnon, III, Takafumi Kato, Rhianna E. Lee, Boyd L. Yount, Teresa M. Mascenik, Gang Chen, Kenneth N. Olivier, Andrew Ghio, Longping V. Tse, Sarah R. Leist, Lisa E. Gralinski, Alexandra Schäfer, Hong Dang, Rodney Gilmore, Satoko Nakano, Ling Sun, M. Leslie Fulcher, Alessandra Livraghi-Butrico, Nathan I. Nicely, Mark Cameron, Cheryl Cameron, David J. Kelvin, Aravinda de Silva, David M. Margolis, Alena Markmann, Luther Bartelt, Ross Zumwalt, Fernando J. Martinez, Steven P. Salvatore, Alain Borczuk, Purushothama R. Tata, Vishwaraj Sontake, Adam Kimple, Ilona Jaspers, Wanda K. O'Neal, Scott H. Randell, Richard C. Boucher, Ralph S. Baric

PII: S0092-8674(20)30675-9

DOI: https://doi.org/10.1016/j.cell.2020.05.042

Reference: CELL 11447

To appear in: *Cell*

Received Date: 24 April 2020

Revised Date: 11 May 2020

Accepted Date: 20 May 2020

Please cite this article as: Hou, Y.J., Okuda, K., Edwards, C.E., Martinez, D.R., Asakura, T., Dinnon III., K.H., Kato, T., Lee, R.E., Yount, B.L., Mascenik, T.M., Chen, G., Olivier, K.N., Ghio, A., Tse, L.V., Leist, S.R., Gralinski, L.E., Schäfer, A., Dang, H., Gilmore, R., Nakano, S., Sun, L., Fulcher, M.L., Livraghi-Butrico, A., Nicely, N.I., Cameron, M., Cameron, C., Kelvin, D.J., de Silva, A., Margolis, D.M., Markmann, A., Bartelt, L., Zumwalt, R., Martinez, F.J., Salvatore, S.P., Borczuk, A., Tata, P.R., Sontake, V., Kimple, A., Jaspers, I., O'Neal, W.K., Randell, S.H., Boucher, R.C., Baric, R.S., SARS-CoV-2 Reverse Genetics Reveals a Variable Infection Gradient in the Respiratory Tract, *Cell* (2020), doi: https://doi.org/10.1016/j.cell.2020.05.042.

COVID-19
human sera

SARS
human sera

Neutralization

SARS-CoV-2-nLuc

SARS-CoV-nLuc

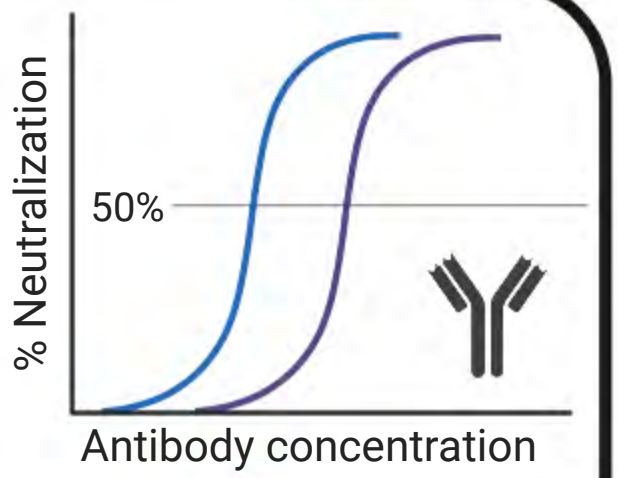

GFP

SARS-CoV-2
cDNA Clone

nLuc

ACE2 expression

Infectivity

Nose

Viral aspiration

Bronchi

Bronchiolar

Alveoli

Lung
infection

Type 1

Type 2

Airway epithelium

Ciliated cells

Alveoli

Type 2

Type 1

SARS-CoV-2 Reverse Genetics Reveals a Variable Infection Gradient in the Respiratory Tract

Yixuan J. Hou[1,19], Kenichi Okuda[3,19], Caitlin E. Edwards[1,19], David R. Martinez[1,19], Takanori Asakura[3], Kenneth H. Dinnon III[2], Takafumi Kato[3], Rhianna E. Lee[3], Boyd L. Yount[1], Teresa M. Mascenik[3], Gang Chen[3], Kenneth N. Olivier[16], Andrew Ghio[17], Longping V. Tse[1], Sarah R. Leist[1], Lisa E. Gralinski[1], Alexandra Schäfer[1], Hong Dang[3], Rodney Gilmore[3], Satoko Nakano[3], Ling Sun[3], M. Leslie Fulcher[3], Alessandra Livraghi-Butrico[3], Nathan I. Nicely[4], Mark Cameron[11], Cheryl Cameron[12], David J. Kelvin[10, 18], Aravinda de Silva[2], David M. Margolis [2,5,6], Alena Markmann[5], Luther Bartelt[5], Ross Zumwalt[13], Fernando J. Martinez[14], Steven P. Salvatore[15], Alain Borczuk[15], Purushothama R.Tata[9], Vishwaraj Sontake[9], Adam Kimple[7], Ilona Jaspers[8], Wanda K. O'Neal[3], Scott H. Randell[3], Richard C. Boucher[3*], Ralph S. Baric[1, 2, 20*]

[1] Department of Epidemiology, University of North Carolina at Chapel Hill, Chapel Hill, NC, USA
[2] Department of Microbiology and Immunology, University of North Carolina at Chapel Hill, Chapel Hill, NC, USA
[3] Marsico Lung Institute, University of North Carolina at Chapel Hill, Chapel Hill, NC, USA
[4] Protein Expression and Purification Core, University of North Carolina at Chapel Hill, Chapel Hill, NC, USA
[5] Department of Medicine, University of North Carolina at Chapel Hill, Chapel Hill, NC, USA
[6]HIV Cure Center, University of North Carolina at Chapel Hill, Chapel Hill, NC, USA
[7] Department of Otolaryngology, University of North Carolina at Chapel Hill, Chapel Hill, NC, USA
[8] Department of Pediatrics, University of North Carolina at Chapel Hill, Chapel Hill, NC, USA
[9] Department of Cell Biology, Regeneration Next Initiative, Duke University Medical Center, Durham, NC, USA
[10] Department of Microbiology and Immunology, Canadian Center for Vaccinology, Dalhousie University, Halifax, NS, Canada
[11] Department of Population and Quantitative Health Science, Case Western Reserve University, Cleveland, OH, USA
[12] Department of Nutrition, Case Western Reserve University, Cleveland, OH, USA
[13] Department of Pathology, University of New Mexico, Albuquerque, NM, USA
[14] Division of Pulmonary and Critical Care Medicine, Joan & Sanford I. Weill Medical College of Cornell University, New York, NY, USA
[15] Department of Pathology, Joan & Sanford I. Weill Medical College of Cornell University, New York, NY, USA

[16] Laboratory of Chronic Airway Infection, Pulmonary Branch, National Heart, Lung, and Blood Institute, National Institutes of Health, Bethesda, MD, USA
[17] National Health and Environmental Effects Research Laboratory, Environmental Protection Agency, Chapel Hill, NC, USA
[18] Laboratory of Immunology, Shantou University Medical College, Shantou, Guangdong, China
[19] These authors contributed equally.
[20] Lead contact

*Correspondence: richard_boucher@med.unc.edu (R.C.B.), rbaric@email.unc.edu (R.S.B.)

Summary

The mode of acquisition and causes for the variable clinical spectrum of COVID-19 remain unknown. We utilized a reverse genetics system to generate a GFP reporter virus to explore SARS-CoV-2 pathogenesis and a luciferase reporter virus to demonstrate sera collected from SARS and COVID-19 patients exhibited limited cross-CoV neutralization. High-sensitivity RNA *in situ* mapping revealed the highest ACE2 expression in the nose with decreasing expression throughout the lower respiratory tract, paralleled by a striking gradient of SARS-CoV-2 infection in proximal (high) vs distal (low) pulmonary epithelial cultures. COVID-19 autopsied lung studies identified focal disease and, congruent with culture data, SARS-CoV-2-infected ciliated and type 2 pneumocyte cells in airway and alveolar regions, respectively. These findings highlight the nasal susceptibility to SARS-CoV-2 with likely subsequent aspiration-mediated virus seeding to the lung in SARS-CoV-2 pathogenesis. These reagents provide a foundation for investigations into virus-host interactions in protective immunity, host susceptibility, and virus pathogenesis.

Introduction

Severe acute respiratory syndrome coronavirus-2 (SARS-CoV-2) has been identified as the causative agent of the ongoing pandemic Coronavirus Disease 2019 (COVID-19) (Gorbalenya et al., 2020). SARS-CoV-2 emerged in Wuhan, China, in December 2019, and rapidly spread to more than 175 countries within three months (Huang et al., 2020; Zhu et al., 2020). As of May 18, 2020, about 4.7 million confirmed cases and >316,000 deaths have been reported worldwide. The absence of approved

vaccines and only a single emergency-use FDA-approved therapeutic against SARS-CoV-2 hinders pandemic control.

The genome of SARS-CoV-2 is a ~30kb RNA predicted to encode 16 non-structural proteins (nsp1-16), four structural proteins (spike, membrane, envelope, and nucleocapsid), and eight accessory proteins (3a, 3b, 6, 7a, 7b, 8b, 9b and 14) (Wu et al., 2020a), expressed from genome length or subgenomic mRNAs. The spike (S) glycoprotein mediates viral entry *via* binding to the human angiotensin-converting enzyme (ACE)-2(Hoffmann et al., 2020; Walls et al., 2020; Yan et al., 2020), followed by proteolytic processing by TMPRSS2, furin, and perhaps other lung proteases, which trigger fusion of viral and cellular membranes. Spike glycoprotein is also the main target of host neutralizing antibodies (nAbs) (Hoffmann et al., 2020).

SARS-CoV-2 infection primarily targets the respiratory tract. A fraction of SARS-CoV-2 infections manifest as bilateral lower-zone pneumonias and diffuse alveolar damage (DAD) that may progress to acute respiratory distress syndrome (ARDS), especially in the aged and individuals with co-morbidities (Carsana et al., 2020; Guan et al., 2020). In comparison to MERS-CoV and SARS-CoV 2003 infections, clinical symptoms of COVID-19 are broader and more variable (Huang et al., 2020; Pan et al., 2020a; Wu and McGoogan, 2020; Zhu et al., 2020). Differences in transmissibility and viral shedding suggest the *in vivo* replication sites and/or replication efficiency of SARS-CoV-2 differ significantly from SARS-CoV (Pan et al., 2020b; Wölfel et al., 2020; Zou et al., 2020).

A wealth of scRNAseq data have been mobilized to describe the expression of ACE2 and TMPRSS2 with emphasis on the human respiratory tract (Aguiar et al., 2020;

Sajuthi et al., 2020; Sungnak et al., 2020). However, complementary techniques are required to describe the organ-level architecture of receptor expression, improve on the sensitivity of scRNA for low expression genes, *e.g.*, ACE2, and to describe the function of ACE2, *i.e.*, mediate infectivity. Accordingly, a combination of RNA *in situ* (ISH) hybridization techniques, a novel set of SARS-CoV-2 reporter viruses produced by reverse genetics, and primary cultures from all affected regions of the respiratory tract was assembled for our investigations.

The reverse genetics systems were utilized to test for protection/durability of protection afforded by convalescent serum and/or SARS-CoV-2-specific monoclonal antibodies (mAbs) and antigenicity relationships between SARS-CoV and SARS-CoV-2 after natural human infections. These tools were also utilized to contrast two non-exclusive hypotheses that may account for key aspects of SARs-CoV-2 transmission and pathogenesis: 1) transmission is mediated by airborne microparticles directly infecting the lung (Morawska and Cao, 2020; Wilson et al., 2020); or 2) the nose is the initial site of infection, followed by aspiration of the viral inoculum from the oropharynx into the lung (Dickson et al., 2016; Wölfel et al., 2020). Accordingly, we characterized the ACE2 and TMPRSS2 expression levels in the nose and lung and in parallel the SARS-CoV-2 infection of human nasal, bronchial, bronchiolar, and alveolar epithelial cultures. These findings were compared with virus distributions and tropisms in lungs from lethal COVID-19 cases.

Results

Recombinant viruses replicate similarly to the SARS-CoV-2 clinical isolate *in vitro*.

A full-length infectious cDNA clone of a US SARS-CoV-2 clinical isolate WA1 was generated by cloning seven genomic fragments separately into vector plasmids (Figure 1A). Additionally, two reporter viruses were constructed by replacing a 276 bp-region in the ORF7 with a green fluorescent protein (GFP) or a GFP-fused nanoluciferase (nLuc) gene (Figure 1A). After assembly into full-length cDNA, full-length RNA was electroporated into Vero-E6 cells (Scobey et al., 2013; Yount et al., 2003). After recovering the wild-type (WT), icSARS-CoV-2-GFP, and icSARS-CoV-2-nLuc-GFP recombinant viruses, viral replication was confirmed by the presence of sub-genomic length leader-containing RNA transcripts 20 hours post-electroporation (Figure S1). All three recombinant viruses replicated (Figure S1), generated similar plaques in Vero E6 cells and could be passaged serially in the cell culture without exogenous trypsin (Figure 1B). Cytopathic effect (CPE) was defined by cell rounding and detachment from monolayers. GFP signals were evident in cells two days post-transfection with RNA transcripts from both indicator viruses (Figure 1C).

To distinguish our recombinant viruses from the circulating SARS-CoV-2 strains, we introduced a silent mutation (T15102A) into a conserved region in nsp12 to ablate an endogenous SacI site in the molecular clone (Figure S1). We confirmed the presence of this mutation in all three recombinant viruses but not in the clinical SARS-CoV-2 isolate by Sanger sequencing and PCR amplification followed by SacI digestion (Figures 1D and 1E). To evaluate viral RNA synthesis, Northern blot analyses were performed that showed that the number of sgRNA bands was equivalent in the recombinant and clinical isolates, confirming the presence of 8 principle subgenomic mRNAs during infection (Figure 1F). As expected, the molecular weights of sgRNA 2 to

7 in the two reporter viral samples were higher than those in the clinical isolate and WT samples, reflecting the insertion of the 720 bp GFP gene or the 1,233 bp nLuc-GFP gene into the 366 bp-ORF7 genetic location. These data also demonstrated that ORF7 was not essential for *in vitro* replication of SARS-CoV-2.

Next, we evaluated one-step (MOI = 5) and multi-step (MOI = 0.05) growth curves of the three recombinant viruses in Vero E6 cells in comparison to the clinical isolate WA1 strain. The titer of all SARS-CoV-2 increased and plateaued to mid 10^6 PFU/mL within 12-18h in the one-step curve and within 36-48h in the multi-step curve (Figures 2A and 2B). In contrast to other reported indicator viruses (Thao et al., 2020), the three recombinant viruses replicated to titers equivalent to the clinical isolate.

Serine Proteases TMPRSS2 and Furin, but not Exogenous Trypsin, Enhance the Replication of SARS-CoV-2.

Host proteases, including cell surface and intracellular proteases, play an essential role in CoV infection by processing the S protein to trigger membrane fusion (Izaguirre, 2019; Matsuyama et al., 2010; Matsuyama et al., 2005; Menachery et al., 2020; Millet and Whittaker, 2014; Wicht et al., 2014). Therefore, we evaluated the multi-step replication (MOI = 0.03) of the icSARS-CoV-2-GFP in the presence of selected proteases via fluorescent microscopy and measurements of viral titer.

Vero cells were infected with the icSARS-CoV-2-GFP reporter virus in the presence of 0, 1, or 5 µg/mL of trypsin. Unlike some coronaviruses (CoVs) (Menachery et al., 2020; Wicht et al., 2014), trypsin did not trigger syncytium formation and at 24/48h, a slightly higher percentage of trypsin-exposed cells expressed GFP signals

and CPE as compared with controls (Figures 2C and S2). Trypsin also resulted in slightly lower virus titers than controls (Figure 2D), suggesting that trypsin impairs the stability of viral particles in supernatants.

SARS-CoV-2 S protein exhibits a novel 4 amino acid furin-cleavage site “RRAR” at the junction between S1 and S2 subunits (Andersen et al., 2020; Coutard et al., 2020). We observed increased icSARS-CoV-2-GFP expression in the furin-overexpressing vs WT cells at 24h (Figure 2E), correlating with one $\log_{10}$ higher infectious titers compared to WT Vero cells at early times after infection (Figure 2F). Moreover, extensive CPE was noted in furin cells vs parental Vero cell cultures (Figure S2). In contrast, enhanced expression of TMPRSS2 in LLC-MK cells resulted in higher levels of GFP expression and higher icSARS-CoV-2-GFP titers (Figures 2G and 2H). These data suggest that serine proteases like furin and TMPRSS2 enhance the replication efficiency/cytopathology of SARS-CoV-2 *in vitro*.

The neutralization sensitivity of SARS-CoV-2 nLuc virus to potent SARS and MERS monoclonal antibodies and polyclonal sera

Three neutralization assays were developed utilizing luciferase reporter CoVs, including SARS-CoV, MERS-CoV, and SARS-CoV-2 (Figure 3A-H). Previous studies have identified remarkably potent SARS and MERS nAbs that target receptor binding domains and exhibit strong neutralizing activities *in vitro* and *in vivo* (Ying et al., 2015; Yu et al., 2015; Zhu et al., 2007). We utilized three highly cross-reactive nAb against SARS-CoV (S230, S230.15, and S227.9), two nAb against MERS-CoV (MERS-27 and m336), and one broadly cross-reactive nAb against Dengue virus (EDE1-C10). We also

tested a pooled mouse serum sample collected from BALB/c mice vaccinated and boosted with a Venezuelan equine encephalitis virus viral replicon particle (VRP-SARS-COV-2-S) encoding the SARS-CoV-2 S gene. The boost was performed three weeks post-vaccination, and sera were collected one week before and one week after boost.

Both the MERS nAbs, MERS-27 and m336, neutralized the icMERS-CoV-nLuc virus but not the 2003 SARS-CoV-nLuc or 2019 SARS-CoV-2-nLuc-GFP recombinant viruses. Similarly, the three SARS nAb, S230, S230.15 and S227.9 exhibited potent neutralization activities against icSARS-CoV-nLuc, but not icSARS-CoV-2-nLuc-GFP (Figures 3A, 3C and 3E). As a negative control, a Dengue virus nAb EDE1-C10 did not neutralize any of the three tested CoVs. Importantly, the mouse serum sample neutralized 99.4% of the icSARS-CoV-2-nLuc-GFP virus at a 1:2 dilution after prime, and much more potent neutralization was noted after VRP-SARS-CoV-2-S boost (Figure 3G).

The S proteins of SARS-CoV and SARS-CoV-2 share 75% identity in amino acid sequences. To investigate whether SARS-CoV and SARS-CoV-2 infections elicit cross-neutralizing antibodies, five serum samples from patients who survived the 2003 SARS-CoV Toronto outbreak and 10 serum sample from COVID-19 survivors were evaluated using nLuc neutralization assays with the two reporter CoVs. All five 2003 SARS serum samples demonstrated high neutralization titers against SARS-CoV-nLuc virus, with half-maximal inhibitory dilution (ID_{50}) activities in the range from 1:30.6 to 1:376.5 (Figure 3F). Surprisingly, two of these serum samples, A and E, neutralized icSARS-CoV-2-nLuc-GFP with 11.9- and 8.1-fold of decreases in ID_{50}, respectively. In contrast, 10 COVID-19 convalescent serum samples displayed variable neutralization ID_{50} titers

that ranged from 61.67 to 782.70 against icSARS-CoV-2-nLuc-GFP but little, if any, neutralization of 2003 icSARS-CoV-nLuc or icMERS-CoV-nLuc viruses at the lowest dilutions tested (Figures 3B, 3D and 3H).

RNA *in situ* hybridization localization of the SARS-CoV-2 receptor complex in the normal human upper and lower respiratory tract.

The sites of SARS-CoV-2 infection in the upper airways (nose, oropharynx) and lung (lower airways, alveoli) are under active investigation (Rockx et al., 2020). Accordingly, we characterized ACE2 and TMPRSS2 expression in these regions using RNA *in situ* hybridization (Figures 4 and S3). Consistent with the low level of ACE2 expression reported from scRNAseq data (Brann et al., 2020; Durante et al., 2020; Sajuthi et al., 2020), low levels of ACE2 were detected in the respiratory epithelium lining the nasal cavity (Figure 4A). Scattered, low levels of ACE2 and TMPRSS2 expression were also observed in the squamous epithelium lining oropharyngeal tonsillar tissue (Figure S3A). Notably, progressively reduced levels of ACE2 expression were observed in the lower airway regions, culminating in minimal levels in the alveolar region. Quantitative comparisons of nasal and bronchial airway epithelia obtained as brush samples simultaneously from the same subjects by qPCR revealed significantly higher expression of ACE2 but not TMPRSS2 in nasal vs bronchial tissues (Figure 4B). In a separate qPCR study, there was a gradient of reduced ACE2 expression from proximal to distal intrapulmonary regions (Figure 4C). In contrast, TMPRSS2 mRNA exhibited an overall higher expression level in all respiratory tract regions than ACE2.

Previously reported scRNAseq data describing ACE2 and TMPRSS2 expression in the upper and lower respiratory system have detected ACE2 in ~5% of total cells interrogated (Deprez et al., 2019; Sajuthi et al., 2020) (Figure 4D). We recently developed a single-cell (cytospin)/RNA-ISH technique that is 5-10x more sensitive at assigning cell type-specific expression patterns than scRNAseq (Okuda et al., 2020, submitted to Nat Med) (Figure 4E). This technique identified ACE2 expression in ~20% of interrogated cells vs ~5% by scRNAseq (Figure 4F). These studies identified the FOXJ1-defined ciliated cell as the most frequent cell type in nasal scrapes (Figure S4B), and that the percentage of ciliated cells expressing ACE2 was higher in the nose than bronchi (Figure 4G). ACE2+, MUC5B+ defined secretory ("club") cells were less frequent and expressed less ACE2 than ciliated cells in each airway region (Figure 4H, I). Both cell types in each region exhibited considerable variability in ACE2 expression (Figures 4H, I). Studies of nasal submucosal glands exhibited few/no detectable ACE2+ glandular cells (Figure S4C). Finally, application of this technique to freshly excised distal lung digests revealed expression of ACE2 in a fraction of AT2 cells (Figure 4Evi). ACE2 was detected in *HOPX*-positive cells, which in humans can be AT1 or AT2 cells (Figure 4Evii) (Ota et al., 2018).

Pre-existing pulmonary disease and ACE2/TMPRSS2 expression.

Suppurative muco-obstructive lung diseases, *e.g.*, cystic fibrosis (CF) and non-CF bronchiectasis (NCFB), are characterized by airways mucus accumulation and neutrophilic inflammation and are reported to be at increased risk for severe SARS-CoV-2 infections (Boucher, 2019; CDC COVID-19 Response Team, 2020). To test

whether dysregulation of ACE2 expression is a feature of CF, RNA-ISH studies were performed in excised CF lungs and revealed a striking upregulation of ACE2 and TMPRSS2 expression in CF airways (Figure 5A).

To gain insight into pathways that may contribute to dysregulation of ACE2 expression in CF lungs, the effects of selected cytokines on ACE2 expression in large airway epithelial (LAE) cultures were tested. IL1β, the dominant pro-mucin secretory cytokine in CF and NCFB secretions (Chen et al., 2019), upregulated ACE2, but not TMPRSS2 (Figure 5Bi). Because CF subjects experience recurrent virus-driven exacerbations, the effect of IFNβ on ACE2 expression was tested. ACE2 expression was significantly increased, whereas TMPRSS2 expression decreased, by IFNβ (Figure 5Bii). In contrast, IL13, a cytokine associated with Th2-high asthma, inhibited ACE2 expression (Figure 5Biii).

Respiratory tract region-specific SARS-CoV-2 infectivity.

To test the relationship between ACE2 entry receptor expression and SARS-CoV-2 infection, we inoculated primary epithelial cultures from the nasal surface epithelia (HNE, n=9 donors), large airway (bronchi, LAE, n=7 donors), lower airway (bronchiolar, SAE, n=3 donors), nasal submucosal glands (n=2 donors), type II- and type I-like pneumocytes (AT2-/AT1-like, n=3 donors), microvascular endothelial cells (MVE, n=2 donors), and fibroblasts (FB, n=2 donors), and an immortalized nasal cell line (UNCNN2TS), with icSARS-CoV-2-GFP reporter virus. We observed GFP signals and detected viral titers in HNE, LAE, SAE, AT2-like and AT1-like cell cultures (Figure 6A). In contrast, nasal submucosal gland, UNCNN2TS, MVE, or FB cells were not

susceptible, as evidenced by no GFP signals or detectable infectious titers of progeny viruses (not shown).

We measured the relative infectivity of the SARS-CoV-2 GFP virus in primary cells based on the average peak titers and observed that infectivity exhibited the same pattern as the ACE2 expression levels from the upper to lower respiratory tract (Figure 6Bi-6Biv). The icSARS-CoV-2-GFP virus replicated efficiently in HNE and LAE, with peak viral titers significantly higher than the titers in SAE, AT2-like and AT1-like cultures (Figure 6Bv). Although the viral peak titers were similar, the icSARS-CoV-2-GFP infection in HNE culture resulted in significantly higher titers than LAE at 24h, 48h and 96h post-infection, suggesting more robust replication in the primary nasal cells (Figure 6Bvi). Collectively, these data indicate that virus infectivity/replication efficiency varies markedly from proximal airway to alveolar respiratory regions.

Whole mount immunohistochemistry of HNE and LAE cultures was utilized to identify cell types infected by SARS-CoV-2 (Figure 6C, S4A). The ciliated cell was routinely infected and extruded. In contrast, the other major cell type facing the airway lumen, *i.e.*, the MUC5B+ club cell, was not infected, nor was the MUC5AC+ metaplastic goblet cell. We did note a cell type co-expressing the ciliated cell marker tubulin and MUC5B was rarely infected in HNE, a finding consistent with infection of a secretory/club cell transitioning to a ciliated cell phenotype.

There is debate whether AT2 and/or AT1 cells express sufficient ACE2 to mediate infection and whether AT2, AT1, or both cell types are infectable. Previous studies reported 2003 SARS-CoV infects AT2 but not AT1 pneumocytes (Mossel et al., 2008). To focus on the relative infectivity by SARS-CoV-2 for AT2 vs AT1 cells,

304 standard AT2/AT1 cell cultures and a novel cell culture approach that well preserves
305 AT2 and AT1 cell populations over the infection/GFP expression interval were tested.
306 As shown in Figure 6A and S4B, AT2 cells appeared to be preferentially infected.
307
308 **Respiratory tract region-specific aspects of SARS-CoV-2 infectivity**
309 We next investigated three other aspects of SARS-CoV-2 infection of human
310 airway epithelia. First, the variability of infectivity among HNE and LAE cultures from
311 multiple donors was characterized. While all nine HNE and seven LAE were infected by
312 icSARS-CoV-2-GFP, marked variability in GFP signals per culture surface area and
313 viral growth curves were observed. LAE cultures exhibited higher variability in
314 susceptible cells than the HNE cultures at 72hpi (Figures 6A, 6B, 6D and S4C). Ciliated
315 cell numbers in five LAE cultures were quantitated, and no correlation was noted
316 between susceptibility and ciliated cell percentages (Figure 6Dii).
317 Second, to further characterize the infectivity of LAE vs SAE, replication rates of
318 three SARS-CoV-2 viruses in LAE and SAE cultures from the same donor were
319 compared. All three viruses replicated more slowly in SAE than LAE cells. The GFP
320 virus replicated modestly less effectively than the clinical isolate or WT virus in the two
321 regions (Figure 6E). This observation differs from the equivalent replication noted in the
322 Vero-E6 cells (Figures 2A and 2B), suggesting an intact ORF7 gene contributes to
323 SARS-CoV-2 replication, and perhaps virulence, in human tissues.
324 Third, the replication of SARS-CoV and SARS-CoV-2 in LAE cells were
325 compared. SARS-Urbani WT and GFP viruses, in parallel with the three SARS-CoV-2
326 viruses, were administered to LAE cultures from the same donor. GFP signals were

detected in LAE cultures for both viruses, but the SARS-CoV-2-GFP exhibited delayed and less intense signals than SARS-CoV-Urbani-GFP (Figure S4D). This phenotype is consistent with the growth curve in which a lower titer of SARS-CoV-2 was recorded at 24h.

SARS-CoV-2 infection in COVID-19 autopsy lungs

We utilized RNA-ISH/IHC to localize virus in four lungs from SARS-CoV-2-infected deceased subjects (Table S1). Multiple observations at different length scales were notable. First, at the macroscopic level, the infection appeared patchy, segmental, and peripheral (Figures 7A and S5A). These characteristics are consistent with an aspiration distribution of an infectious inoculum. Second, ciliated cells within the superficial epithelia lining proximal airway surfaces, particularly the trachea, were infected (Figure 7B and S5B). As observed *in vitro*, MUC5B+ club and MUC5AC+ goblet cells were not infected *in vivo*. Third, the submucosal glands that populate the large airway regions of the lung were not infected (Figure S5C). Fourth, alveolar cells were also infected. RNA *in situ* and IHC co-localization of an AT2 cell marker, SPC (*SFTPC*) and AT1 cell marker (AGER) with SARS-CoV-2 indicated that AT2 cells and AT1 cells (or AT2 cells that had transitioned to AT1 cells) were infected (Figure 7C and S5D).

During the routine AB-PAS staining that detects mucins/mucin-like carbohydrates in SARS-CoV-2-infected autopsy lungs, we noted faint AB-PAS staining in the peripheral lung, *i.e.*, alveolar region in some lungs (Figures 7D). Because aberrant mucin secretion and accumulation is a feature of parenchymal diseases that can

progress to fibrosis, the AB-PAS material was characterized in more detail (Figures 7Dii-7Dv). IHC studies suggested that this material in large airways was a mixture of the secreted mucins MUC5B and MUC5AC (Figure 7Div). In the alveolar parenchymal region, MUC5B alone was detected and was enriched in the peripheral subpleural area, as often observed in idiopathic pulmonary fibrosis (IPF) (Figure 7Dv) (Evans et al., 2016). Note, in none of the autopsy lungs studied was mechanical ventilation employed and the lung in panels A and D of Figure 7 was immersion fixed. These observations, coupled to the observation that MUC5AC was not detected in the peripheral region, makes it unlikely that MUC5B selectively was mechanically spread from central to peripheral lung zones.

Discussion

We generated a SARS-CoV-2 reverse genetics system, characterized virus RNA transcription profiles, evaluated the impact of ectopically expressed proteases on virus growth, and used reporter viruses to characterize virus tropisms, *ex vivo* replication, and to develop a high-throughput neutralizing assay. These reagents were utilized to explore aspects of early infectivity and disease pathogenesis relevant to SARS-CoV-2 respiratory infections.

Our RNAscope/cytospin technology extended the description of ACE2 in respiratory epithelia based on scRNAseq data (Sungnak et al., 2020). RNA/cytospin detected ~20% of upper respiratory cells expressing ACE2 vs ~4% for scRNAseq (Figure 4F). Most of the RNA-ISH-detected ACE2-expressing cells were ciliated cells, not normal MUC5B+ secretory (club) cells or goblet cells. Notably, the nose contained

the highest percentage of ACE2-expressing ciliated cells in the proximal airways (Figure 4G). The higher nasal ACE2 expression-level findings were confirmed by qPCR data comparing nasal to bronchial airway epithelia. qPCR data also revealed that ACE2 levels further waned in the more distal bronchiolar and alveolar regions. Importantly, these ACE2 expression patterns were paralleled by high SARS-CoV-2 infectivity of nasal epithelium with a gradient in infectivity characterized by a marked reduction in the distal lung (bronchioles, alveoli) (Figures 6A and 6B).

Multiple aspects of the variability in SARS-CoV-2 infection of respiratory epithelia were notable in these studies. First, significant donor variations in virus infectivity and replication efficiency were observed. Notably, the variability was less in the nose than lower airways. The reason(s) for the differences in lower airway susceptibility are important but remain unclear (Cockrell et al., 2018). We identified variations in ACE2 receptor expression (Figures 4A-D) but not numbers of ciliated cells as potential variables (Figure 6D). Second, variation in infectivity of a single cell type, *i.e*., the ciliated cell, was noted with only a fraction of ciliated cells having access to virus infected at 72 h (Figure 6A). Third, the dominant secretory cell, *i.e.*, the MUC5B+ club cell, was not infected *in vitro* or *in vivo*, despite detectable ACE2 and TMPRSS2 expression (Figures 4G-4I). Collectively, these data suggest that measurements of ACE2/TMPRSS2 expression do not fully describe cell infectivity and that a description of other variables that mediate susceptibility to infection, including the innate immune system(s), is needed (Menachery et al., 2014).

The ACE2 receptor gradient in the normal lung raised questions focused on the initial sites of respiratory tract virus infection, the mechanisms that seed infection into

the deep lung, and the virus-host interaction networks that attenuate or augment intra-regional virus growth in the lung to produce severe disease, especially in vulnerable patients experiencing chronic lung or inflammatory diseases (Guan et al., 2020; Leung et al., 2020).

We speculate that nasal surfaces may be the dominant initial site for SARS-CoV-2 respiratory tract infection (Wölfel et al., 2020). First, SARS-CoV-2 RNA has been detected in aerosol particles in the range of aerodynamic sizes exhaled during normal tidal breathing (Liu et al., 2020; Papineni and Rosenthal, 1997). Aerosol deposition and fomite mechanical delivery deposition modeling suggest that aerosols containing virus inhaled by naïve subjects achieve the highest density of deposition, *i.e.*, highest MOI per unit surface area, in the nose (Booth et al., 2005; Farzal et al., 2019; Teunis et al., 2010). Second, the relatively high ACE2 expression in nasal specimens and the parallel high infectivity of the HNE cultures suggests the nasal cavity is a fertile site for early SARS-CoV-2 infection. Nasal infection likely is dominated by ciliated cells in the superficial epithelium, not nasal submucosal glands. Third, the nose is exposed to high but variable loads of environmental agents, producing a spectrum of innate defense responses. Hence, a portion of the variability of the clinical syndrome of COVID-19 may be driven by environmentally driven variance nasal infectivity (Wu et al., 2020b).

Another aspect of the variability of the COVID-19 syndrome is the variable incidence and severity of lower lung disease. It is unlikely SARS-CoV-2 is transmitted to the lung by hematogenous spread, as demonstrated by the absence of infection of MVE cells and previous reports that indicate airway cultures are difficult to infect from the basolateral surface (Sims et al., 2005; Wölfel et al., 2020). Theoretically, infection could

be transmitted directly to lower lung surfaces by microaerosol inhalation with deposition on and infection of alveolar surfaces mediated in part by the high ACE2 binding affinity reported for SARS-CoV-2 (Shang et al., 2020; Wrapp et al., 2020). However, given the low levels of ACE2 expression in alveolar cells in health, the correlated poor infectivity *in vitro*, and the absence of a homogeneous pattern radiographically, the importance of this route remains unclear (Santarpia et al., 2020).

In contrast, it is well-known that an oral–lung aspiration axis is a key contributor to many lower airways infectious diseases (Dickson et al., 2016; Esther et al., 2019; Gaeckle et al., 2020; Odani et al., 2019; Phillips et al., 2015). Nasal secretions are swept from the nasal surface rostrally by mucociliary clearance and accumulate in the oral cavity at a rate of ~0.5 ml/hr where they are admixed with oropharyngeal/tonsillar fluid (Eichner et al., 1983; Pandya and Tiwari, 2006). Especially at night, it is predicted that a bolus of relatively high titer virus is aspirated into the deep lung, either via microaspiration or as part of gastro-esophageal reflex-associated aspiration, sufficient to exceed the threshold PFU/unit surface area required to initiate infection (Amberson, 1954; Gleeson et al., 1997; Huxley et al., 1978). Note, our data that tracheas exhibited significant viral infection *in vivo* suggest that small-volume microaspiration could also seed this site. Tracheal-produced virus could then also accumulate in the oropharynx via mucus clearance for subsequent aspiration into the deep lung (Quirouette et al., 2020). Oropharyngeal aspirates also contain enzymes and/or inflammatory mediators that may condition alveolar cells for infection. Aspiration of SARS-CoV-2 into the lung is consistent with the patchy, bibasilar infiltrates observed by chest CT in COVID-19 (Xu et al., 2020). Notably, robust microaspiration and gastro-esophageal aspiration are

observed frequently in subjects who are at risk for more severe COVID-19 lower respiratory disease, *e.g.*, older, diabetic, and obese subjects (Pan et al., 2020a; Phillips et al., 2015). Finally, our autopsy studies demonstrated patchy, segmental/subsegmental disease, consistent with aspiration of virus into the lung from the oropharynx.

These speculations describing the early pathogenesis of SARS-CoV-2 upper and lower respiratory tract disease are consistent with recent clinical observations. The data from Wölfel et al. (2020) in COVID-19-positive subjects support the concept of early infection in the upper respiratory tract (0-5 d) followed by subsequent aspiration and infection of the lower lung. These authors focused on the oropharynx as a potential site of the early virus propagation. As noted above, however, a nasal-oropharyngeal axis also exists which has two implications. First, the nasal surfaces could seed the oropharynx for infection. Second, it is likely that oropharyngeal secretions reflect a mixture of local secretions admixed with a robust contribution of nasal mucus and virus.

Animal model data are also compatible with the scenario of aspiration-induced focal SARS-CoV-2 lung disease. The data of Rockx et al. (2020) noted focal lung disease after combined intranasal/intratracheal dosing with SARS-CoV-2 in cynomolgus monkeys. Notably, other findings in this model phenocopied our observations of human disease, *e.g.*, early nasal shedding of virus, infection of nasal ciliated cells, and infection of AT2 and likely AT1 cells. Perhaps more definitive data describing nasal cavity seeding of the lower lung by microaspiration emanate from the studies of Richard et al. (2020). These investigators demonstrated in ferret models that genetically marked virus

464 delivered to the nasal cavity more efficiently transmitted infection to the lower lungs than
465 a virus with a distinct genetic marker delivered directly into the lungs.

466 In addition to identifying possible microaspiration risk factors associated with
467 COVID-19 disease severity in the elderly, diabetic, and obese, our studies provide
468 insights into variables that control disease severity in subjects at risk due to pre-existing
469 pulmonary disease (Leung et al., 2020; Sajuthi et al., 2020). For example, ACE2
470 expression was increased in the lungs of CF patients excised at transplantation. A
471 major cytokine that produces the muco-inflammatory CF airways environment, IL1β,
472 was associated *in vitro* with increased ACE2 expression (Chen et al., 2019). The clinical
473 outcome of increased ACE2 expression in CF is not yet known. The simple prediction is
474 that increased ACE2 expression might be associated with more frequent/severe SARS-
475 CoV-2 disease in CF populations. However, increased ACE2 expression is reported to
476 be associated with improved lung function by negatively regulating ACE and the
477 angiotensin II and the angiotensin II type 1a receptor (AT1a) in models of alveolar
478 damage/pulmonary edema and bacterial infection (Imai et al., 2005; Jia, 2016; Keeler et
479 al., 2018; Kuba et al., 2005; Sodhi et al., 2019). Consequently, CF subjects might
480 exhibit reduced severity of disease once acquired. Data describing outcomes of COVID-
481 19 in the CF populations should emerge soon (Colombo et al., 2020).

482 Our autopsy studies also provide early insights into the variable nature of the
483 severity and pathogenesis related to post-COVID-19 lung health/function (Atri et al.,
484 2020; Kollias et al., 2020; Magro et al., 2020). Our study has identified another feature
485 of COVID-19, *i.e.*, the accumulation of apparently aberrantly secreted MUC5B in the
486 alveolar region. Accumulation of MUC5B in the peripheral/alveolar lung is characteristic

of subjects who develop idiopathic pulmonary fibrosis (IPF), and polymorphisms in the MUC5B promoter associated with IPF have been reported (Evans et al., 2016). Future studies of the long-term natural history of SARS-CoV-2 survivors, in combination with studies delineating the cell types responsible for MUC5B secretion (AT2 vs airway cells) and genetics, *e.g.*, MUC5B polymorphisms, may aid in understanding the long-term favorable vs fibrotic outcomes of COVID-19 disease (Chan et al., 2003; Rogers et al., 2018).

Our study also provides a SARS-CoV-2 infectious full-length cDNA clone for the field. Several strategies have been developed to construct stable coronavirus molecular clones, including the bacterial artificial chromosome (BAC) (Almazan et al., 2000; Gonzalez et al., 2002) and vaccinia viral vector systems (Casais et al., 2001). In contrast, our *in vitro* ligation method solves the stability issue by splitting unstable regions and cloning the fragmented genome into separate vectors, obviating the presence of a full-length genome (Yount et al., 2000). Our *in vitro* ligation strategy has generated reverse genetic systems for at least 13 human and animal coronaviruses and produced hundreds of mutant recombinant viruses (Beall et al., 2016; Menachery et al., 2015; Scobey et al., 2013; Xie et al., 2020; Yount et al., 2003). In contrast to other reports (Thao et al., 2020), reporter recombinant SARS-CoV-2 viruses generated herein replicated to normal WT levels in continuous cell lines, allowing for robust ex vivo studies in primary cultures.

Using this infectious clone, we generated a high-throughput luciferase reporter SARS-CoV-2 assay for evaluation of viral nAbs. In line with previous reports (Tian et al., 2020; Wrapp et al., 2020), our data show that several SARS-CoV RBD-binding nAbs fail

to neutralize SARS-CoV-2, suggesting distant antigenicity within the RBD domains between the two viruses. Although more samples are needed, early convalescent sera demonstrated ~1.5 logs variation in neutralizing titers at ~day 30 post-infection, demonstrating a need to fully understand the kinetics, magnitude, and durability of the neutralizing antibody response after a primary SARS-CoV-2 infection. The detection of low level SARS-CoV-2 cross-neutralizing antibodies in 2003 SARS-CoV serum samples is consistent with recent studies (Hoffmann et al., 2020; Walls et al., 2020), suggesting that existence of common neutralizing epitopes between the two CoVs. Interestingly, convalescent COVID-19 sera failed to cross-neutralized SARS-CoV *in vitro*, suggesting cross-neutralizing antibodies may be rare after SARS-CoV-2 infection. The location of these epitopes is unknown. The nLuc recombinant viruses described herein will be powerful reagents for defining the antigenic relationships between the Sarbocoviruses, the kinetics and durability of neutralizing antibodies after natural infection, and the breadth of therapeutic neutralizing antibodies and vaccine countermeasures (Wang et al., 2019).

In summary, our studies have quantitated differences in ACE2 receptor expression and SARS-CoV-2 infectivity in the nose (high) vs the peripheral lung (low). These studies should provide valuable reference data for future animal models development and expand the pool of tissues, *e.g.*, nasal, for future study of disease pathogenesis and therapy. While speculative, if the nasal cavity is the initial site mediating seeding of the lung via aspiration, these studies argue for the widespread use of masks to prevent aerosol, large droplet, and/or mechanical exposure to the nasal passages. Complementary therapeutic strategies that reduce viral titer in the nose early

in the disease, *e.g.*, nasal lavages, topical antivirals, or immune modulation, may be beneficial. Finally, our studies provide key reagents and strategies to identify type specific and highly conserved neutralizing antibodies that can be assessed most easily in the nasal cavity as well as in the blood and lower airway secretions.

Acknowledgments

We would like to acknowledge the following funding sources from the National Allergy and Infectious Disease (NIAID), National Institution of Health (NIH) to R.S.B. (**U19-AI100625, R01-AI089728, U01-AI14964**), and National Heart, Lung, and Blood institute (NHLBI), NIH to R.C.B. (**UH3-HL123645, P01-HL110873, R01-HL136961, P30-DK065988-13, P01-HL108808**). K.O. is funded by the Cystic Fibrosis Foundation (OKUDA10I0) and a research grant from Cystic Fibrosis Research Incorporation. D.R.M. is funded by an NIH NIAID T32 AI007151 and a Burroughs Wellcome Fund Postdoctoral Enrichment Program Award. T.K. is funded by a Senior Research Training Fellowship (RT-57362) of American Lung Association. A.J.K is support by National Center for Advancing Translational Sciences, NIH, through grant # KL2TR002490. We thank N. J. Thornburg at CDC for providing us the SARS-CoV-2 clinical isolate WA1 strain. We are grateful for the technical support of Y. Escobar for HNE cultures and Lisa Morton for qPCR assays; by S. Weiss, Y. Park, J. Kuruc and UNC Blood Donor Center on COVID-19 serum sample preparation. The UNC Animal Histopathology & Laboratory Medicine Core is supported in part by an NCI Center Core Support Grant (5P30CA016086-41) to the UNC Lineberger Comprehensive Cancer Center. We thank

E. C. Roe for assisting manuscript editing. Finally, we are grateful for the donors of primary cells and sera who made this study possible.

Author Contributions

Conceptualization R.C.B., R.S.B and S.H.R.; Investigation: Y.J.H., K.O., C.E.E., D.R.M., T.A., K.D.3, T.K., R.L., B.L.Y., T.M.M., G.C., K.N.O., A.G., L.V.T., S.R.L., L.E.G., A.S., H.D., R.G.,S.N., L.S., L.F., W.K.O., S.H.R.; Contribution to research materials: A.L.B., N.I.N., M.C., C.C., D.J.K., A.D.S., D.M.M., A.M., L.B., R.Z., F.J.M., S.P.S., A.B., P.R.T., A.K., I.J., S.H.R., Writing – original draft preparation: Y.J.H.; Writing – review and editing: R.C.B., R.S.B., S.H.R and W.K.O.; Visualization: Y.J.H., K.O., C.E.E., D.R.M., T.A., T.K.; Funding acquisition: R.C.B. and R.S.B.

Declaration of Interests

The authors declare no competing financial interests.

Figure legends

Figure 1. See also Figure S1. Design and recovery of SARS-CoV-2 recombinant viruses. (A) Full-length cDNA clone constructs and genomes of recombinant viruses. Restriction sites, cohesive ends, and the genetic marker T15102A (*) are indicated in the schematic diagram. GFP or GFP-fused nLuc genes were introduced into the ORF7 (replacing aa # 14-104) of SARS-CoV-2 genome. (B) Plaques of recombinant viruses. (C) CPE and GFP signals were observed in Vero-E6 cells electroporated with sgRNA-N

578 alone (mock) or sgRNA-N mixed with full-length RNA transcripts (recombinant viruses)
579 at two days post-transfection. Scale bar = 100 μm. SacI digestion (D) and Sanger
580 sequencing (E) of a 1.5kb region covering the genetic marker in vial genomes. (F).
581 Northern blot analysis of genomic and sub-genomic (sg) RNAs isolated from the virus-
582 infected cells. Isolate: Clinical isolate strain WA1; WT: icSARS-CoV-2-WT; GFP:
583 icSARS-CoV-2-GFP; nLuc-GFP: icSARS-CoV-2-nLuc-GFP.
584
585 **Figure 2. See also Figure S2. Growth curves and the role of proteases in SARS-**
586 **CoV-2 replication.** (A) One-step and (B) multi-step growth curves of clinical isolate and
587 recombinant viruses in Vero E6 cells, with MOI of 5 and 0.05, respectively. Fluorescent
588 images (C) and viral titers (D) of the SARS-CoV-2-GFP replicates in Vero cells
589 supplemented with different concentrations of trypsin. Fluorescent images (E) and viral
590 titers (F) of the SARS-CoV-2-GFP replicates in normal Vero or Vero-furin cells.
591 Fluorescent images (G) and viral titers (H) of the SARS-CoV-2-GFP replicates in normal
592 LLC-MK or LLC-MK-TMPRSS2 cells. All scale bars = 200 μm. Data are presented in
593 mean ± SD.
594
595 **Figure 3. Neutralization assays using luciferase reporter coronaviruses.** (A) mAbs
596 and (B) COVID-19 sera against icMERS-CoV-nLuc; (C) mAbs and (D) SARS and
597 COVID-19 sera against icSARS-CoV-nLuc; (E) mAbs, (F) SARS and COVID-19 sera,
598 and (F) vaccinated mouse serum against icSARS-CoV-2-nLuc-GFP; (H) ID_{50} values of
599 SARS and COVID-19 sera cross-neutralizing SARS-CoV and SARS-CoV-2. The same
600 sera samples are indicated with arrows. MERS-CoV neutralizing mAbs: MERS-27,

m336; SARS-CoV neutralizing mAbs: S230, S230.15, S227.9; Dengue virus mAb: EDE1-C10; SARS patient serum samples: A to E; COVID-19 patient serum samples: 1 to 10; mouse serum was produced by immunized BALB/c mice with SARS-CoV-2 spike.

Figure 4. Intraregional *ACE2* and *TMPRSS2* mRNA expression in normal human airways. See also Figure S3. (A) Representative RNA *in situ* hybridization (ISH) images demonstrating regional distribution of *ACE2* and *TMPRSS2* mRNA localization (red signal) in normal human airway surface epithelium. Scale bars=20 μm. (B) Comparison of *ACE2* and *TMPRSS2* mRNA expression between matched nasal and bronchial brushed tissues obtained from 7 healthy subjects. (C) Relative expression of *ACE2* and *TMPRSS2* mRNA in different airway regions enriched for epithelial cells, including tracheas, bronchi, bronchiole, and alveoli, obtained from matched 7 normal lungs. (D) Frequency of *ACE2* and *TMPRSS2*-positive cells among total cells identified in distinct anatomical airway regions in a reanalysis of scRNA-seq data (Deprez. M *et al*., BioRxiv, 2019). (E) RNA-ISH images depicting mRNA expression of *ACE2* and cell type markers, including *FOXJ1* (ciliated) (Ei, ii, and iv), *MUC5B* (secretory) (Eiii and v), *SFTPC* (alveolar type 2) (Evi), and *HOPX* (alveolar type 1 or 2) (Evii) on cytospins of nasal/bronchial superficial epithelial and purified alveolar cells. Scale bars=10 μm. (F) Frequency of *ACE2*-positive cells among nasal and bronchial preparations. A total of 1,000 cells were analyzed for *ACE2* expression per donor (N=3). G. Frequency of *ACE2*-positive cells among *FOXJ1*+ or *MUC5B*+ cells in nasal or bronchial preparations. A total of 200 *FOXJ1*+ or *MUC5B*+ cells were analyzed for *ACE2* expression per donor (N=3). H, I. Histograms depicting number of dot signals of *ACE2* expression in *FOXJ1*

or *MUC5B*+ cells in nasal (H) or bronchial (I) preparations identified by scRNA-ISH. *ACE2*-positive dot signals were counted in 200 *FOXJ1* or *MUC5B*-positive cells per donor (N=3). Statistics for B, C, F and G used linear mixed-effect model with donor as random-effect factor for comparison between groups, and pair-wise comparisons of groups with more than 2 levels were performed using Tukey post-hoc tests. H and I used generalized linear mixed-effect models with Poisson distribution to compare the difference in cell counts at varying *ACE2* expression levels between *FOXJ1*+ and *MUC5B*+ cells. Histobars and error bars represent mean ± SD. Different symbol colors indicate results from different individual donors.

Figure 5. Inflammatory cytokines alter *ACE2* and *TMPRSS2* expression. (A) RNA *in situ* hybridization images demonstrating regional distribution of *ACE2* and *TMPRSS2* mRNA localization in normal and CF human airways. Scale bars = 20 μm. Images were obtained from four different airway regions from one normal or CF subject as representative of N=6 normal or CF subjects studied. (B) mRNA expression of *ACE2* and *TMPRSS2* measured by Taqman assay after inflammatory cytokine challenge in primary human large airway epithelial cells. Bi. IL1β (10 ng/ml, 7 days, N=8). Bii. IFNβ (10 ng/ml, 3 days, N=4 donors, 2-3 cultures/donor). Biii. IL13 (10 ng/ml, 7 days, N=8). Wilcoxon matched-pairs signed rank test was used for comparison between control and cytokine treatment groups. Histobars and error bars represent mean ± SD. Different symbol colors indicate results from different individual donors.

Figure 6. See also Figure S4. Replication of SARS-CoV-2 in primary human respiratory cells. (A) Representative GFP signals in icSARS-CoV-2-GFP-infected HNE, LAE, SAE, AT2-like and AT-1 like culture at 48h. Scale bar = 80. (B) Growth curves of icSARS-CoV-2-GFP in (i) HNE, n = 9 donors; (ii) LAE, n = 7 donors; (iii) SAE, n = 3 donors; (iv) AT1-like (empty symbols) and AT2-like (filled symbols) cells, n = 3 donor/each. Cells from female and male donors are labeled in pink and blue, respectively. Triplicated viral infection under MOI of 3 and 0.5 are shown in solid and dotted lines, respectively. (v) Comparison of the highest titers of individual culture among cell types; (vi) Comparison of individual titers in HNE and LAE at different time points. (C) Representative whole-mount extended focus views of icSARS-CoV-2-GFP-infected HNE and LAE cell cultures. Red = filamentous actin (phalloidin), White = α-tubulin (multiciliated cells), Green = GFP (virus), Blue = nuclei (Hoechst 33342). Yellow = MUC5B (left). Yellow = MUC5AC (right). Arrow: viral infected α-tubulin+ (ciliated) / MUC5B+ (secretory) transitional HNEs. Scale bars = 50 μm. (D) (i) Variability of GFP and cilia signals in icSARS-CoV-2-GFP-infected LAE cultures collected from five different donors at 72hpi, scale bar = 200 μm. (ii) Quantification of ciliated area in the LAE cultures. (E) Growth curves of icSARS-CoV-2-GFP infected in LAE and SAE collected form the same donor. Cultures were infected with SARS-CoV-2 clinical isolate (i), WT (ii) and GFP (iii) with MOI of 0.5. Data are presented in mean ± SD.

Figure 7. Characterization of cell types for SARS-CoV-2 infection in SARS-CoV-2 autopsy lungs. See also Figure S5. (A) Sections from of an autopsy lung with SARS-CoV-2 infection were stained by hematoxylin and eosin (i) and probed for SARS-CoV-2

669 by RNA *in situ* hybridization (ISH) (ii-iv). SARS-CoV-2 sense probe (ii) was used as a
670 negative control. Scale bars = 1 mm. (B) The trachea from a SARS-CoV-2 autopsy was
671 probed for SARS-CoV-2 by RNA ISH. (i) Colorimetric detection of SARS-CoV-2 (red)
672 showing infection of surface epithelium. (ii-iv) Co-localization of SARS-CoV-2 (red) with
673 cell-type-specific markers (green) determined by dual-immunofluorescent staining (Bii,
674 acetylated α-tubulin cilia marker; Biii, MUC5B secretory cell marker; and Biv, MUC5AC
675 mucous/goblet-cell marker). Scale bars = 10 μm. (C) Co-localization of SARS-CoV-2
676 with alveolar cell-type-specific markers in the alveolar space from a SARS-CoV-2
677 autopsy. (i) Dual color-fluorescent RNA ISH co-localization of SARS-CoV-2 (green) with
678 alveolar type II cell marker *SFTPC* (red). (ii) Dual-immunofluorescent co-localization of
679 SARS-CoV-2 (green) with alveolar type I cell marker AGER (magenta). Scale bars = 20
680 μm. (D) Mucin expression in SARS-CoV-2 autopsy lung. (i) Alcian Blue-periodic acid–
681 Schif (AB-PAS; blue to purple) stain for complex carbohydrate (mucin); (ii) MUC5B
682 immunohistochemistry; (iii-v) dual-immunofluorescent staining for MUC5B (green) and
683 MUC5AC (red) in the large airway (iv) and the alveoli (v). SMG = submucosal grand.
684 Scale bars = 2mm (i-iii); 200 μm (iv and v).
685
686 **STAR Methods**
687 **RESOURCE AVAILABILITY**
688 **Lead Contact**
689 Further information and requests for resources and reagents should be directed to and
690 will be fulfilled by the Lead Contact, Ralph S. Baric (rbaric@email.unc.edu).
691

692 **Materials Availability**

693 Material and reagents generated in this study will be made available upon installment of
694 a material transfer agreement (MTA).

695

696 **Data and Code Availability**

697 Genomic sequences of recombinant viruses icSARS-CoV-2-WT, icSARS-CoV-2-GFP
698 and icSARS-CoV-2-nLuc-GFP, which were generated in this study, have been
699 deposited to GenBank (Accession # MT461669 to MT461671).

700

701 **EXPERIMENTAL MODEL AND SUBJECT DETAILS**

702 **Human Subjects**

703 Excess surgical pathology tissues were obtained from the University of North Carolina
704 (UNC) Tissue Procurement and Cell Culture Core under protocol #03-1396 approved by
705 the UNC Biomedical IRB. Informed consent was obtained from tissue donors or
706 authorized representatives. Cystic fibrosis lung tissue was obtained from donors
707 undergoing transplantation, while human lungs from previously healthy individuals
708 unsuitable for transplantation were obtained from Carolina Donor Services (Durham, NC),
709 the National Disease Research Interchange (Philadelphia, PA), or the International
710 Institute for Advancement of Medicine (Edison, NJ). Upper airway tissues were obtained
711 from subjects undergoing elective surgeries. Excised tissue specimens were dissected
712 and fixed in 10% neutral buffered formalin for 48 hours followed by paraffin-embedding.
713 The paraffin blocks were cut to produce 5 μm serial sections for RNA-ISH and
714 immunohistochemistry. For qRT-PCR for *ACE2* and *TMPRSS2* expression in nasal and

715 bronchial epithelial cells, nasal and bronchial epithelial cells were obtained from
716 matched healthy volunteers by nasal scraping and bronchoscopic brush-biopsy under
717 the National Heart, Lung, and Blood Institute IRB-approved protocol #07-H-0142. For
718 single cell-RNA *in situ* hybridization (scRNA-ISH), human bronchial epithelial cells were
719 obtained from the left main bronchus of healthy non-smoker volunteers by bronchoscopic
720 brush-biopsy under the UNC Biomedical IRB-approved protocol #91-0679. Nasal surface
721 epithelial cells were isolated from the resected nasal tissues as previously described
722 (Fulcher and Randell, 2013; Okuda et al., 2019). After the isolation of nasal surface
723 epithelial cells, the remaining nasal tissues were micro-dissected to isolate submucosal
724 glands under the light microscope. Donor demographics was shown in Table S1, S2.

725 Tissue blocks or cut sections obtained from four COVID-19 autopsy lungs were
726 obtained from Drs. Ross. E. Zumwalt (University of New Mexico) and Steven Salvatore
727 and Alain Borczuk (New York Presbyterian Hospital). Donor demographics were
728 described as below.

729 Donor 1. 40-year-old, male. Medical history: Diabetes mellitus. Clinical course:
730 This donor had upper respiratory infection (URI) symptoms three days before he was
731 found dead at home. No intubation was conducted. Postmortem testing of the lung was
732 positive for SARS-CoV-2.

733 Donor 2. 64-year-old, male. Medical history: Diabetes mellitus, diabetic
734 nephropathy, hepatitis C, heart failure, and coronary artery disease. Clinical course:
735 This donor was transferred to ER because of fever and respiratory distress. Nasal swab
736 was positive for SARS-CoV-2. He died five hours after urgent care. No intubation was
737 conducted.

Donor 3. 95-year-old, female. Medical history: Hypertension, hyperlipidemia, Alzheimer's disease. Clinical course: This donor was transferred to ER because of respiratory distress. Nasal swab was positive for SARS-CoV-2. She died 48 hours after urgent care. No intubation was conducted.

Donor 4. 69-year-old, male. Medical history: acute myeloid leukemia, type 2 diabetes mellitus. Clinical course: This donor was admitted to the hospital because of respiratory distress eight days after initial URI symptoms and diagnosis of SARS-CoV-2. He died five days post admission. No intubation was conducted.

Primary Cell Culture

Primary human nasal epithelial cells (HNE) were collected from healthy volunteers by curettage under UNC Biomedical IRB-approved protocols (#11-1363 and #98-1015) after informed consent as previously described (Kesic et al., 2011; Knowles et al., 2014). Briefly, superficial scrape biopsies were harvested from the inferior nasal turbinates under direct vision through a 9 mm reusable polypropylene nasal speculum (Model 22009) on an operating otoscope with speculum (Model 21700). Both nostrils were scraped 5 times without anesthesia using a sterile, plastic nasal curette (Arlington Scientific). Nasal cells were expanded using the conditionally reprogrammed cell (CRC) method (Gentzsch et al., 2017) or in Pneumacult EX Plus media (Stem Cell Technologies) (Speen et al., 2019) and then cultured on porous Transwell (Corning) supports in Pneumacult air liquid interface (ALI) media (Stem Cell Technologies). Human bronchial epithelial [large airway epithelial (LAE)] and bronchiolar [small airway epithelial (SAE)] cells, human alveolar type II pneumocytes (AT2), and human primary

761 lung microvascular endothelial cells (MVE) and fibroblasts (FB) were isolated from
762 freshly excised normal human lungs obtained from transplant donors with lungs
763 unsuitable for transplant under IRB-approved protocol (#03-1396), as previously
764 described (Fulcher and Randell, 2013; Okuda et al., 2019).
765
766 **Cell Lines**
767 Simian kidney cell lines Vero (ATCC # CCL81), Vero E6 (ATCC # CRL1586), and LLC-
768 MK (ATCC# CCL-7) were purchased from ATCC and preserved in our laboratory. The
769 Vero-furin cell line was reported previously (Mukherjee et al., 2016). LLC-MK cells
770 expressing TMPRSS2 were generated in our laboratory. A novel immortalized nasal cell
771 line (UNCNN2TS) was created by lentiviral over expression of Bmi-1 and hTERT
772 (Fulcher et al., 2009) in primary nasal cells, and subsequent lentiviral addition of SV40 T
773 antigen (pBSSVD2005 was a gift from David Ron, Addgene plasmid # 21826).
774 UNCNN2T cells are grown and infected in EpiX media (Propagenix).
775
776 **Virus strains**
777 Clinical SARS-CoV-2 isolate WA1 strain was provided by Dr. Natalie J. Thornburg at the
778 U.S. Centers for Disease Control and Preventive (CDC). The virus was isolated from
779 the first US COVID-19 patient identified in Washington state (GenBank Accession#:
780 MT020880). Recombinant CoVs icSARS-CoV-Urbani, icSARS-CoV-GFP, icSARS-CoV-
781 nLuc and icMERS-CoV-nLuc were generated in our laboratory as described previously
782 (Scobey et al., 2013; Yount et al., 2003). Briefly, the strategy to synthesize full-length
783 cDNA clones for SARS-CoV-Urbani and MERS-CoV was identical to the method

reported herein, but with different restriction sites and junctions. The GFP and nLuc reporters were inserted into the accessory ORF7a of the icSARS-CoV-Urbani clone, whereas the nLuc reporter gene was introduced into the accessory ORF5a of the icMERS-CoV clone. Virus stocks were propagated on Vero E6 cells in minimal essential medium containing 10% fetal bovine serum (HyClone) and supplemented with penicillin/kanamycin (Gibico). Virus plaques were visualized by neutral red staining at two days post-infection. The UNC Institutional Biosecurity Committee and the National Institute of Allergy and Infectious Disease (NIAID) have approved the SARS-CoV-2 molecular clone project. All viral infections were performed under biosafety level 3 (BSL-3) conditions at negative pressure, and Tyvek suits connected with personal powered-air purifying respirators.

Human serum samples

SARS serum samples were obtained from SARS convalescent patients from University Health Network, MaRS Center, Toronto, Canada that had a confirmed SARS infection under IRB-approved protocol (#UHN REB 03-0250). COVID-19 serum samples were also provided as coded material and were deemed "not human subject research" by the UNC School of Medicine Biomedical IRB (#20-1141).

METHOD DETAILS

Primary human cell culture and infection

Nasal cells were expanded using the conditionally reprogrammed cell (CRC) method (Gentzsch et al., 2017) or in Pneumacult EX Plus media (Stem Cell Technologies)

(Speen et al., 2019) and then cultured on porous Transwell (Corning) supports in Pneumacult air liquid interface (ALI) media (Stem Cell Technologies). Human LAE and SAE cells were cultured as previously described (Fulcher and Randell, 2013; Okuda et al., 2019). Briefly, Isolated LAE and SAE cells were co-cultured with mitomycin-treated 3T3 J2 cells on collagen-coated tissue culture plastic dishes in DMEM media supplemented with 10 μM Y-27632 (Enzo Life Science). At 70-90% confluence, LAE and SAE cells were passaged and sub-cultured for expansion. P2 LAE and SAE cells were transferred to human placental type IV collagen-coated, 0.4 μm pore size Millicell inserts (Millipore, PICM01250). The LAE and SAE cells were seeded at a density of 2.8 × 10^5 cells/cm^2 and cultured in UNC ALI media. Upon confluence, cells were maintained at an ALI by removing apical media and providing UNC ALI media to the basal compartment only. Medium was replaced in the basal compartment twice a week, and the apical surfaces were washed with PBS once a week. After 28 days, LAE and SAE cells were utilized for SARS-CoV-2 recombinant viruses infection. Human type II pneumocytes (AT2) were prepared and cultured on porous supports as previously described (Bove et al., 2010). The AT2 cells are grown in DMEM with P/S and 10% FBS and switched to 4% FBS 24 hours prior to infection. Cells were studied within three days and after five days, as they transdifferentiate into type I pneumocyte (AT1)-like cells. For serum-free and feeder-free AT2 cell cultures (mixed AT1/AT2 culture), human lung pieces (~2gm) were washed twice with PBS containing 1% Antibiotic-Antimycotic and cut into small pieces. Visible small airways and blood vessels were carefully removed to avoid clogging. Then samples were digested with 30 ml of enzyme mixture (collagenase type I: 1.68 mg/ml, dispase: 5U/ml, DNase: 10U/ml) at 37°C for 45 min with rotation.

The cells were filtered through a 100 µm strainer and rinsed with 15 ml PBS through the strainer. The supernatant was removed after centrifugation at 450x g for 10 min and the cell pellet was resuspended in red blood cell lysis buffer for five minutes, washed with DMEM/F12 containing 10% FBS and filtered through a 40 µm strainer. To purify human AT2 cells, approximately two million total lung cells were resuspended in SF medium and incubated with Human TruStain FcX (BioLegend) followed by incubation with HTII-280 antibody (Terrace Biotech). The cells were washed with PBS and then incubated with anti-mouse IgM microbeads. The cells were loaded into LS column (Miltenyi Biotec) and labeled cells collected magnetically. HTII-280^{+} human AT2 cells (1-3 × 10^{3}) were resuspended in culture medium. Serum-free feeder free medium and AT2 differentiation medium will be described elsewhere (S.V. and PRT et al., currently under revision in Cell Stem Cell). Culture plates were coated with Cultrex reduced growth factor basement membrane extract, Type R1 and cultured for five days followed by changing medium to AT2 differentiation medium for additional five days.

Human primary lung microvascular endothelial cells (MVE) and fibroblasts (FB) were grown as previously described (Scobey et al., 2013). For MVE cells, peripheral lung tissue minus the pleura was minced, digested with dispase/elastase, and cells were grown in EGM-2 media plus FBS (Lonza). Two or three rounds of CD31 bead purification (Dynabeads; Life Technologies) resulted in >95% CD31-positive cells by flow cytometry that were used between passages 5 and 10. FBs were obtained by finely mincing distal human lung tissue and plating on scratched type 1/3 collagen-coated dishes in Dulbecco's modified Eagle medium with high glucose (DMEMH) media plus 10% FBS, antibiotics, and antimycotics. Cells were released using trypsin/EDTA and

subcultured in DMEMH, 10% FBS and P/S. The subcultured cells were elongated, spindly and negative for CD31 and pan-cytokeratin by flow cytometry and immunofluorescence, respectively.

icSARS-CoV-2-GFP virus infections were performed using well differentiated air-liquid interface (ALI) cultures of five donor specimens of human nasal epithelial (HNE) and large airway epithelial (LAE) cells using an MOI of three. Small airway epithelial (SAE) cell ALI cultures were created as previously described (Okuda et al., 2019). Paired LAE / SAE cells were inoculated with a SARS-CoV-2 clinical isolate, icSARS-CoV-2-WT, and icSARS-CoV-2-GFP, as well as wild-type icSARS-CoV-Urbani and icSARS-CoV-GFP on LAE, using an MOI of 0.5 for each virus. Transwell-cultured primary cells were inoculated with 200ul of virus v*ia* the apical surface and allowed to incubate at 37°C for two hours. Following incubation, virus was removed, and cells were washed twice with 500ul PBS. Cells were returned to 37°C for the remainder of the experiment and observed for fluorescent signal, when appropriate, every 12-24 hours. 100ul PBS was added to the apical surface of each culture and allowed to incubate for 10 minutes at 37°C in order to obtain an apical wash sample, at time points for analysis of viral replication by plaque assay. At the last time point, cells were lysed with 500ul TRIzol reagent (Invitrogen) to obtain total final RNA for analysis.

Primary human bronchial epithelial cell culture and cytokines exposure: Primary human LAE cells from normal donors (obtained from donors without previously known pulmonary diseases) were cultured on the human placenta collagen IV (Sigma Cat#C-7521) coated transwell (Corning Cat#3640) under air-liquid interface (ALI) condition.

The apical surface was washed with PBS, and ALI medium (Fulcher et al., 2009) was replaced only in the basal compartment two-three times per week, and cells were cultured under ALI conditions for four weeks to allow full differentiation. Exposure with recombinant human cytokines was administrated started at the 5th week after ALI culture. All recombinant human cytokines (IL1β at 10ng/ml, IL13 at 10ng/ml, and IFNβ at 10ng/m of final concentration in ALI media) were added to basolateral side of ALI media, and media were changed after three days supplied with freshly diluted cytokines. Cells were collected at day five – day seven for RNA isolation.

Whole-mount immunostaining and imaging.

Well-differentiated mock or icSARS-CoV-2-GFP-infected LAE ALI cultures were fixed twice for 10 minutes in 4% formaldehyde in PBS and washed and stored in PBS. The GFP signal was enhanced by staining with anti-GFP antibody (Abcam ab6556; 0.5 ug/mL), a Venezuelan equine encephalitis virus (VEEV)-like replicon particle-immunized mouse antiserum against SARS-CoV-2 N protein (1:4000 dilution) and polyclonal rabbit anti-SARS-CoV N protein (Invitrogen PA1-41098, 0.5 ug/mL) using species-specific secondary antibodies as previously described (Ghosh et al., 2018). The cultures were also imaged for α-tubulin (Millipore MAB1864; 3ug/mL), MUC5AC (ThermoScientific 45M1; 4ug/mL), MUC5B [polyclonal rabbit against a MUC5B peptide (MAN5BII), 1:1000] (Thornton et al., 2000), and CCSP (Sigma 07-623; 1:2000) as indicated. Filamentous actin was localized with phalloidin (Invitrogen A22287), and DNA with Hoechst 33342 (Invitrogen). An Olympus FV3000RS confocal microscope in Galvo scan mode was used to acquire 5-channel Z stacks by 2-phase sequential scan. Representative stacks

were acquired with a 60X oil objective (xyz = 212um x 212um x ~25um), and are shown as Z-projections or single-slice, XZ cross sections to distinguish individual cell features and to characterize the infected cell types. A 20X objective was used to acquire 2D, single-channel, apical snapshots of nine fields (636um x 636um; combined area = 3.64mm^2), selected in evenly spaced grids across each sham infected donor culture, and ImageJ was used to measure the relative apical culture surface covered by multiciliated cells.

Immunohistochemistry

Immunohistochemical staining was performed on COVID-19 autopsy lung sections according to a protocol as previously described (Okuda et al., 2019). Briefly, paraffin-embedded sections were baked at 60 °C for 2–4 hours, and deparaffinized with xylene (2 changes × 5 min) and graded ethanol (100% 2 × 5 min, 95% 1 × 5 min, 70% 1 × 5 min). After rehydration, antigen retrieval was performed by boiling the slides in 0.1 M sodium citrate pH 6.0 (3 cycles with microwave settings: 100% power for 6.5 min, 60% for 6 min, and 60% for 6 min, refilling the Coplin jars with distilled water after each cycle). After cooling and rinsing with distilled water, quenching of endogenous peroxidase was performed with 0.5% hydrogen peroxide in methanol for 15 min, slides washed in PBS, and blocked with 4% normal donkey serum, for an hour at RT. Primary antibody (MUC5AC: 45M1, 1:1000, MUC5B: H300, 1:1000, SARS-CoV-2 nucleocapsid: 1:500, Anti-SARS mouse antiserum: 1:4000, Acetylated-α-tubulin: 1:1000, AGER: 1:400) were diluted in 4% normal donkey serum in PBST and incubated over night at 4 °C. Mouse and rabbit gamma globulin was used as an isotype control at the same

concentration as the primary antibody. Sections were washed in PBST and secondary antibodies (biotinylated donkey anti-rabbit IgG, at 1:200 dilution in 4% normal donkey serum in PBST for chromogenic DAB staining for MUC5B, Alexa Fluor 488 donkey anti-rabbit IgG, at 1:1000 dilution and Alexa Fluor 594 donkey anti-mouse IgG, at 1:1000 dilution for fluorescent staining) were applied for 60 min at RT. After washing in PBST, the Vector® TrueVIEW Autofluorescence Quenching Kit (Vector laboratories) was used to reduce background staining, and glass coverslips were placed over tissue sections with the ProLong Gold Antifade Reagent with DAPI (Invitrogen) for fluorescent staining. For chromogenic DAB staining, slides were incubated with avidin-peroxidase complex according to the manufacturer's instructions (Vectastain kit, Vector laboratories), washed, incubated with the chromogenic substrate (Immpact Novared, Vector laboratories) and counterstained with Fast Red. Coverslipped slides were scanned and digitized using an Olympus VS120 whole slide scanner microscope with a 40X/60X 0.95 NA objective and Olympus confocal microscope with a 40X 0.6 NA or 60X 1.4 NA objective.

Cell dissociation for single cell-RNA *in situ* hybridization (scRNA-ISH)

Fresh bronchoscopically brush-biopsied human main bronchial epithelial cells, nasal surface epithelial and submucosal gland cells isolated from the resected nasal tissues were incubated with Accutase solution for 30 min at 37°C. The Accutase-treated cells were centrifuged (450 g, 2 min, 4°C) and then incubated with 10 mL HBSS (Ca+, Mg+) buffer containing DNase I (0.1 mg/ml) (Roche #10104159001) and collagenase IV (1 mg/ml) (Gibco #17104-019) for 10 min and 30 min for bronchial/nasal surface epithelial

cell and nasal submucosal gland cell isolation, respectively at 37°C with intermittent agitation. Nasal submucosal glands were micro-dissected from the nasal tissues under microscopy. The tissues were centrifuged (450 g, 2 min, 4°C) and then incubated with 10 mL HBSS (Ca+, Mg+) buffer containing DNase I (0.1 mg/ml) and collagenase IV (1 mg/ml) for 30 min at 37°C with intermittent agitation followed by additional incubation with Trypsin-EDTA (Final concentration: 0.125%, Gibco #25200-056) for 20 min at 37°C. After incubation, enzymes were inactivated by adding 500 µL fetal bovine serum. Dissociated cells were filtered through a 40-µm cell strainer, centrifuged (450 g, 2 min, 4°C) and resuspended in PBS, adjusted to 10^5 cells/ml. Cell viability was examined by trypan blue dye exclusion. Single cell suspension was cytocentrifuged (55 g, 4 min, StatSpin CytoFuge2, Beckman Coulter) and fixed in 10% NBF for 30 min at room temperature. The cytocentrifuged cells were washed with PBS three times and then dehydrated with graded ethanol (50% 1 min, 70% 1 min, 100% 1 min). The slides were stored in 100% ethanol at -20°C until future use for scRNA-ISH.

RNA *in situ* hybridization

RNA-ISH was performed on cytocentrifuged single cells using the RNAscope Multiplex Fluorescent Assay v2, and on paraffin-embedded 5 µm tissue sections using the RNAscope 2.5 HD Reagent Kit and RNAscope 2.5 HD Duplex Reagent Kit according to the manufacturer's instructions (Advanced Cell Diagnostics). Cytospin slides were rehydrated with graded ethanol (100% 1 min, 70% 1 min, 50% 1 min), permeabilized with PBS + 0.1% Tween 20 (PBST) at RT for 10 min, incubated with hydrogen peroxide (Advanced Cell Diagnostics) at RT for 10 min, followed by incubation with 1:15 diluted

protease III at RT for 10 min. Tissue sections were deparaffinized with xylene (2 changes × 5 min) and 100% ethanol (2 changes × 1 min), and then incubated with hydrogen peroxide for 10 min, followed by target retrieval in boiling water for 15 min, and incubation with Protease Plus (Advanced Cell Diagnostics) for 15 min at 40 °C. Slides were hybridized with custom probes at 40 °C for 2 hours, and signals were amplified according to the manufacturer's instructions. The stained sections were scanned and digitized using an Olympus VS120 light or fluorescent microscope with a 40X 1.35 NA objective and Olympus confocal microscope with a 40X 0.6 NA or 60X 1.4 NA objective.

Calculation of frequency of *ACE2* and *TMPRSS2*-positive cells in distinct anatomical airway regions as identified by scRNA-seq

Normalized log-transformed count+1 gene x cell matrix and meta-data were downloaded from https://www.genomique.eu/cellbrowser/HCA/, which represent 77,969 cells that passed quality control. Expression of *ACE2* and *TMPRSS2* were extracted from the matrix, and the number of cells with log normalized count > 0 were calculated.

RNA isolation and gene expression analysis by Taqman Assays

For qRT-PCR for *ACE2* and *TMPRSS2* expression in different airway regions, surface epithelial cells were isolated from freshly excised normal human lungs obtained from transplant donors by gentle scraping with a convex scalpel blade into F12 medium, excluding submucosal glands. Following centrifugation (450 g, 5 min, 4 °C), the pelleted epithelial cells were resuspended in 1 ml of TRI Reagent (Sigma). Micro-dissected small

991 airways and peripheral lung parenchyma were homogenized in 1 ml of TRI Reagent
992 using a tissue homogenizer (Bertin Technologies). Debris was pelleted from the TRI
993 Reagent by centrifugation, and the supernatant was used for RNA analysis.

994 The HBE cells growing on the transwell membrane were collected by excision of
995 the whole membrane together with the cells using razor blade and lysed in TRI Reagent
996 at 37°C shaker for 30 minutes. Total RNA was purified from the TRI Reagent lysates
997 using the Direct-Zol RNA miniprep Kit (Zymo Research, cat#R2051), and examined by
998 NanoDrop One Spectrophotometer (ThermoFisher) for its quality and quantity. 1μg of
999 total RNA was reverse transcribed to cDNA by iScript™ Reverse Transcription
1000 Supermix (BioRad, Cat#1708840) at 42°C for one hour. Quantitative RT-PCR was
1001 performed using Taqman probes (Applied BioSystems) with SsoAdvanced Universal
1002 Probes Supermix (Bio-Rad, cat#1725280) on QuantStudio6 Real-time PCR machine
1003 (Applied Biosystem). The house-keeping gene used for normalization of gene
1004 expression for *in vitro* cultured HBE was TATA-binding protein (TBP) gene. See Key
1005 Resource Table for detailed information about primers/probes.
1006

1007 **Assembly of SARS-CoV-2 WT and reporter cDNA constructs**

1008 Seven cDNA fragments covering the entire SARS-CoV-2 WA1 genome were amplified
1009 by RT-PCR using PrimeSTAR GXL HiFi DNA polymerase (TaKaRa). Junctions between
1010 each fragment contain non-palindromic sites BsaI (GGTCTCN^NNNN) or BsmBI
1011 (CGTCTCN^NNNN) with unique four-nucleotide cohesive ends. Fragment E and F
1012 contains two BsmBI sites at both termini, while other fragments harbor BsaI sites at the
1013 junction. Four-nucleotide cohesive ends of each fragment are indicated in Figure 1A. To

assist the transcription of full-length viral RNA, we introduced a T7 promoter sequence into the upstream of fragment A, as well as a 25nt poly-A tail into the downstream of the fragment G. Each fragment was cloned into high-copy vector pUC57 and verified by Sanger sequencing. A silent mutation T15102A was introduced into a conserved region in nsp12 in plasmid D as a genetic marker. To enhance the efficiency of recovering SARS-CoV-2 virus in the cell culture, a sgRNA-N construct, encoding a 75nt leader sequence, N gene, 3'UTR, and a 25nt poly-A tail, was assembled under the control of a T7 promoter. Two reporter viruses, one containing GFP and the other harboring, a GFP-fused nLuc gene, were generated by replacing the ORF7 gene with the reporter genes.

Generation of full-length RNA transcript and recovery of recombinant viruses

Seven genomic cDNA fragments were digested with appropriate endonucleases, resolved on 0.8% agarose gels, excised and purified using a QIAquick Gel Extraction kit (Qiagen). A full-length genomic cDNA was obtained by ligating seven fragments in an equal molar ratio with T4 DNA ligase (NEB). We then purified the ligated cDNA with chloroform and precipitated it in isopropanol. The full-length viral RNA or SARS-CoV-2 sgRNA-N were synthesized using the T7 mMESSAGE mMACHINE T7 transcription kit (Thermo Fisher) at 30℃ for 4h. The full-length SARS-CoV-2 transcript and sgRNA-N were mixed and electroporated into 8×10^6 of Vero E6 cells. The cells were cultured as usual in the medium for two to three days.

PCR of leader-containing sgRNAs

Viral replication in the electroporated cells was evaluated by amplification of leader sequence-containing sgRNAs. A forward primer targeting the leader sequence (5'-GTTTATACCTTCCCAGGTAACAAACC -3') was paired with a reverse primer targeting M gene (5'- AAGAAGCAATGAAGTAGCTGAGCC -3') or N gene (5'-GTAGAAATACCATCTTGGACTGAGATC -3').

Identification of the genetic marker

To confirm that the introduced T15102A mutation exists in the recombinant viruses, viral RNA was extracted using TRI Reagent (Thermo Fisher). A 1579 bp fragment in nsp12 of each virus was amplified by RT-PCR using primer pair 5'-GCTTCTGGTAATCTATTACTAGATAAACG-3' and 5'-AAGACATCAGCATACTCCTGATTAGG -3'. The fragment was subjected to Sanger sequencing or digested with SacI enzyme (NEB).

Northern Blot Analysis

Vero E6 cells were infected with SARS-CoV-2 isolate, icSARS-CoV-2-WT, icSARS-CoV-2-GFP or icSARS-CoV-2-GFP-nLuc at an MOI of 1. At 24hr post-infection, we extracted the total cellular RNA using TRIzol Reagent (Thermo Fisher). Poly A-containing messenger RNA was isolated from the total RNA using an Oligotex mRNA Mini Kit (Qiagen). Messenger RNA (0.6-0.7μg) was separated on an agarose gel and transferred to BrightStar-Plus membrane using a NorthernMax-Gly Kit (Invitrogen). Blots were hybridized with a biotin-labeled oligomer (5'-BiodT/GGCTCTGTTGGGAATGTTTTGTATGCG/BiodT-3'), then detected using a

Chemiluminescent Nucleic Acid Detection Module (Thermo Fisher) using the iBright Western Blot Imaging System (Thermo Fisher).

Generation of SAR-CoV-2 S protein-immunized mouse serum

The SAR-CoV-2 S and N genes was cloned into pVR21 3526 to generate virus replicon particles (VRPs), as previously described (Agnihothram et al., 2018). Briefly, SARS-CoV-2 S or N genes were inserted into pVR21, a vector encoding the genome of a VEEV strain 3526. The SARS-CoV-2-S-pVR21 construct, a plasmid containing the VEEV envelope glycoproteins, and a plasmid encoding the VEEV capsid protein were used to generate T7 RNA transcripts. The RNA transcripts were then electroporated into BHK cells. VRPs were harvested 48 hours later and purified via high-speed ultra-centrifugation. Two groups of 10-week-old BALB/c mice (Jackson Labs) were then inoculated with the VRPs via footpad injection then boosted with the same dose once four weeks later. Serum samples were collected at 2 weeks post-boosting and were mixed together.

Monoclonal antibody large-scale production

SARS-specific S230, S230.15, S227.14, S227.9 IgG, MERS-specific MERS-27, m336 IgG, and a Dengue-specific EDE1-C10 IgG antibody variable heavy and light chain genes were obtained, codon-optimized for human mammalian cell expression, and cloned into heavy and light-chain variable-gene-expressing plasmids encoding a human IgG1 Fc region as described previously (Martinez et al., 2020). One hundred μg of each variable heavy and light chain plasmids were co-transfected using an ExpiFectamine

293 transfection kit in Expi293F (Thermo) cells at 2.5 million cells/ml in 1L flasks in suspension. Transfected cell supernatants were harvested two days later, and the soluble antibody was purified using Pierce protein A beads (Thermo) followed by fast protein liquid chromatography (FPLC). MAbs were buffer exchanged with sterile 1XPBS. Purified mAbs were quality controlled by Western blotting and Coomassie blue staining to confirm mAb purity.

MERS-CoV, SARS-CoV, and SARS-CoV-2 neutralization assays

Recombinant viruses icMERS-CoV-nLuc, icSARS-CoV-nLuc, and icSARS-CoV-2-nLuc-GFP were tittered in Vero E6 cells to obtain a relative light units (RLU) signal of at least 20X the cell only control background. Vero E6 cells were plated at 20,000 cells per well the day prior in clear bottom black-walled 96-well plates (Corning 3904). Neutralizing antibody serum samples were tested at a starting dilution of 1:20 and mAb samples were tested at a starting dilution 50μg/ml and were serially diluted 4-fold up to eight dilution spots. icMERS-CoV-nLuc, icSARS-CoV-nLuc, and icSARS-CoV-2-nLuc-GFP viruses were diluted and were mixed with serially diluted antibodies. Antibody-virus complexes were incubated at 37°C with 5% CO2 for 1 hour. Following incubation, growth media was removed, and virus-antibody dilution complexes were added to the cells in duplicate. Virus-only controls and cell-only controls were included in each neutralization assay plate. Following infection, plates were incubated at 37°C with 5% CO2 for 48 hours. After the 48 hours incubation, cells were lysed, and luciferase activity was measured via Nano-Glo Luciferase Assay System (Promega) according to the manufacturer specifications. MERS-CoV, SARS-CoV, and SARS-CoV-2 neutralization

titers were defined as the sample dilution at which a 50% reduction in RLU was observed relative to the average of the virus control wells.

QUANTIFICATION AND STATISTICAL ANALYSIS

For comparison of gene expression in response to cytokine exposure versus control (PBS) with one culture per code in each group, we performed Wilcoxon matched-pairs signed rank test by Graphpad Prism 8 built in function. For comparison of gene expression in response to cytokine exposure vs control (PBS) with more than one culture per code in each group, the linear mixed-effect models analysis were performed. The relative mRNA expression from Taqman assays were analyzed with linear mixed-effect models using the R package *lme4* (Bates et al., 2015), with treatment as fixed effect and code as random-effect factors. Statistical significance were evaluated with the R lmerTest package (Kuznetsova et al., 2017), using the Satterthwarte's degrees of freedom method. Multiple post-hoc comparisons of subgroups were performed using the R multcomp package (Hothorn T, 2008). For cell count data, generalized linear mixed-effect models (glmer) with Poisson distribution was used. Wilcoxon rank sum test was used to determine the statistical significance between unpaired two groups in Figure 2 (D, F and H), and Figure 6 Bvi using Graphpad Prism 8. One-way ANOVA followed by Tukey test was used to determine the statistical significance between groups in Figure 6Bv using Graphpad Prism 8. The "n" numbers for each experiment are provided in the text and figures. $P < 0.05$ was considered statistically significant.

Co-localization of *ACE2* mRNA with marker-genes and quantification

RNA-ISH was performed on cytocentrifuged single cells using RNAscope Multiplex Fluorescent Assay v2, as described above, to assess colocalization of *ACE2* mRNA and airway epithelial cell markers, including *FOXJ1* (ciliated cells) and *MUC5B* (secretory cells). *ACE2* probe (channel 1) was combined with each of airway epithelial cell marker (channel 2). The stained cytospin slides were scanned and digitized using an Olympus VS120 whole slide scanner microscope with a 40X 0.9 numerical aperture objective. Using Fiji software (Schindelin et al., 2012), quantification for colocalization was performed in the scanned images by an investigator blinded to slide identification. To calculate the occurrence of *ACE2*+ cells in preparations, *ACE2*+ cells and total cells were manually counted, and the frequency calculated. For quantitative co-localization analysis of *ACE2* with airway epithelial marker-defined cells, the number of visible *ACE2* signals (dots) was manually counted in each airway epithelial cell-marker-positive cell. The *ACE2*+ signals were quantitated in 200 *FOXJ1*+ *or MUC5B*+ cells per subject. One or more dot signals defined a*n ACE2*+ positive cell, while airway-epithelial-marker-positive cells were defined as cells expressing 10 or more dot signals for the epithelial marker.

Quantification of *ACE2* and *TMPRSS2* gene expression in tonsillar surface epithelium

Human tonsil tissue sections were analyzed for *ACE2* and *TMPRSS2* expression using RNA-ISH. Tonsillar surface epithelial regions with positive RNA ISH signals (4 to 8 regions per donor) were selected for quantification. Signal counts were normalized to the number of cells as determined by DAPI nuclear stain in each region. For

quantification, the stratified epithelial layer was divided into two layers: 1) surface (flattened epithelial) layer and 2) basal (cuboidal epithelial) layer.

Supplemental Information

Figure S1. Additional information for the SARS-CoV-2 infectious cDNA clone, Related to Figure 1. (A) Electrophoresis of seven restriction enzyme-digested infectious cDNA clone plasmids. Plasmid A was digested with NotI and BsaI; plasmids B, C, and D were digested with BsaI; plasmids E and F were digested with BsmBI; plasmid G was digested with SalI and BsaI. (B) Amplification SARS-CoV-2 sgRNAs using primers targeting sgRNA-5 (M) and -9 (N). Cellular RNA samples were collected from Vero-E6 cells electroporated with viral RNA transcripts at 20h. Mock cells were electroporated with SARS-CoV-2 sgRNA-9 alone. (C) Alignment of sequences containing the T #15102 in nsp12 gene among 9 different group 2b CoVs.

Figure S2. Cytopathic effect of cells infected with icSARS-CoV-GFP virus, Related to Figure 2. (A) Infected Vero cells supplemented with different concentrations of trypsin. (B) Infected Vero or Vero-furin cells. (C) Infected LLC-MK or LLC-MK-TMPRSS2 cells. All scale bars = 200 μm.

Figure S3. *ACE2* and *TMPRSS2* expression in human tonsillar epithelium and nasal surface epithelium and submucosal glands, Related to Figure 4 (A) Tonsillar surface squamous epithelium stained with (Ai) H&E staining and (Aii) dual-color-fluorescence RNA-ISH showing *TMPRSS2* (green) and *ACE2* (red) along with nuclear staining (blue). Scale bars = 50 um. (iii) Enlarged images of Aii showing surface (iii) and basal (iv) expression; scale bars = 20um. Images are representative from N=3 tonsils,

N=4-8 regions per tonsil. (Av) Signal dots for *ACE2* and *TMPRSS2* mRNAs were counted and normalized to the number of cells in surface and basal layer of tonsillar surface epithelium as described in the STAR methods. Each bar represents the average of N=4-8 regions for each tonsil studied. (B) Frequency of *FOXJ1*- or *MUC5B*-positive cells identified by RNA-ISH among total nasal surface epithelial cells isolated. A total of 1,000 cells were analyzed for *FOXJ1* or *MUC5B* expression per donor. N=3. (C) Cytospins of nasal submucosal glands cells probed by dual-color-immunofluorescent RNA-ISH. Ci shows lack of *ACE2* in *MUC5B*-positve nasal gland cells, while Cii depicts occasional co-expression of *TMPRSS2* in a subset of *MUC5B*-positive cells. Scale bars = 20 μm. (Ciii) Frequency of detection of *ACE2* or *TMPRSS2* positive cells in *MUC5B* positive cells from nasal glands. N=1 gland preparation, a total of 200 *MUC5B* positive cells were counted.

Figure S4. Additional data of SARS-CoV and SARS-CoV-2 infected primary human cells, Related to Fig.6. (A) Representative whole-mount extended focus views of icSARS-CoV-2-GFP-infected (i) HNE and LAE cell cultures. Red = filamentous actin (phalloidin), White = α-tubulin (multiciliated cells), Blue = nuclei (Hoechst 33342). Green = GFP (left). Green = SARS-CoV-2 Nucleocapsid (right). Yellow = MUC5AC (left). Yellow = MUC5B (right); (ii) LAE and SAE cell cultures. Yellow = filamentous actin (phalloidin), White = α-tubulin (multiciliated cells), Blue = nuclei (Hoechst 33342). Green = GFP (virus). Red = CCSP. Scale bars = 50 μm. (B) Merged of GFP and bright field mages taken from AT1 and AT2 cells infected with icSARS-CoV-2-GFP at 48h. The AT-1 cells are present inside the enclosed areas. Bar = 100 μm. (C) GFP signals of

1200 icSARS2-GFP-infected HNEs collected from five different donors at 72hpi, MOI = 3. (D)
1201 (i) Fluorescent signals of the two viruses in LAE (ii) Growth curves of three SARS-CoV-
1202 2 viruses in LAE from the same donor. Scale bar = 200 μm. (iii) Growth curves of two
1203 SARS-Urbani viruses in LAE. All the infections in this figure were in MOI = 0.5.
1204
1205 **Figure S5. SARS-CoV-2 infection in SARS-CoV-2 autopsy lungs, Related to Figure**
1206 **7.** (A) Sections from of a second region of an autopsy lung with SARS-CoV-2 infection
1207 were stained by hematoxylin and eosin (H&E) (i) and probed for SARS-CoV-2 by RNA
1208 *in situ* hybridization (ISH) (ii, iii, and iv). Related to Figure 7A. (B) Frequency of
1209 acetylated alpha tubulin, MUC5AC, or MUC5B colocalization with SARS-CoV-2 positive
1210 cells in the trachea from a SARS-CoV-2 autopsy. A total of 200 randomly selected
1211 SARS-CoV-2 positive cells were analyzed for each dual staining condition. Related to
1212 Figure 7B ii, iii, iv. (C) Absence of SARS-CoV-2 infection in submucosal glands (SMG).
1213 (Ci-ii) H&E staining (i) and RNA-ISH (ii) for SARS-CoV-2 (red) in a large cartilaginous
1214 airway of one autopsy lung. SARS-CoV-2 is only present in the surface epithelium near
1215 the lumen, not in SMG. (Ciii-iv) H&E (iii) and dual-immunofluorescence staining using
1216 acetylated alpha tubulin (red) and anti-SARS-CoV-2 rabbit polyclonal antibody (green)
1217 (iv) from the trachea of a separate autopsy. Related to Figure 7B and S5Di. (D)
1218 Regional distribution of SARS-CoV-2 RNA from trachea to alveoli identified by RNA-ISH
1219 in one SARS-2-CoV autopsy lung (in i and ii, viral staining is red; in iii, viral staining is
1220 turquoise). RNA-ISH dual color images demonstrate SARS-CoV-2 RNA and *SFTPC*
1221 mRNA (alveolar type 2 cell marker) localization in alveoli of a SARS-CoV-2 autopsy

lung. SARS-CoV-2 (turquoise) was identified in a *SFTPC* (red)-positive (iii, arrow) and a *SFTPC*-negative cell (iv, arrowhead); Scale bars = 2mm (A); 100 μm (C); 20 μm (D).

References

Agnihothram, S., Menachery, V.D., Yount, B.L., Jr., Lindesmith, L.C., Scobey, T., Whitmore, A., Schafer, A., Heise, M.T., and Baric, R.S. (2018). Development of a broadly accessible Venezuelan equine encephalitis virus replicon particle vaccine platform. J. Virol. *92*.

Aguiar, J.A., Tremblay, B.J.-M., Mansfield, M.J., Woody, O., Lobb, B., Banerjee, A., Chandiramohan, A., Tiessen, N., Dvorkin-Gheva, A., Revill, S.*, et al.* (2020). Gene expression and in situ protein profiling of candidate SARS-CoV-2 receptors in human airway epithelial cells and lung tissue. bioRxiv, http://dx.doi.org/10.1101/2020.04.07.030742.

Almazan, F., Gonzalez, J.M., Penzes, Z., Izeta, A., Calvo, E., Plana-Duran, J., and Enjuanes, L. (2000). Engineering the largest RNA virus genome as an infectious bacterial artificial chromosome. Proc. Natl. Acad. Sci. U.S.A. *97*, 5516-5521.

Amberson, J.B. (1954). A clinical consideration of abscesses and cavities of the lung. Bull. Johns Hopkins Hosp. *94*, 227-237.

Andersen, K.G., Rambaut, A., Lipkin, W.I., Holmes, E.C., and Garry, R.F. (2020). The proximal origin of SARS-CoV-2. Nat. Med. *26*, 450-452.

Atri, D., Siddiqi, H.K., Lang, J., Nauffal, V., Morrow, D.A., and Bohula, E.A. (2020). COVID-19 for the cardiologist: a current review of the virology, clinical epidemiology, cardiac and other clinical manifestations and potential therapeutic strategies. JACC Basic Transl. Sci., http://dx.doi.org/10.1016/j.jacbts.2020.04.002.

Bates, D., Mächler, M., Bolker, B., and Walker, S. (2015). Fitting linear mixed-effects models using lme4. J. Stat. Softw. *67*, 1-48.

Beall, A., Yount, B., Lin, C.M., Hou, Y., Wang, Q., Saif, L., and Baric, R. (2016). Characterization of a pathogenic full-length cDNA clone and transmission model for porcine epidemic diarrhea virus strain PC22A. mBio *7*, e01451-01415.

Booth, T.F., Kournikakis, B., Bastien, N., Ho, J., Kobasa, D., Stadnyk, L., Li, Y., Spence, M., Paton, S., Henry, B.*, et al.* (2005). Detection of airborne severe acute respiratory syndrome (SARS) coronavirus and environmental contamination in SARS outbreak units. J. Infect. Dis. *191*, 1472-1477.

Boucher, R.C. (2019). Muco-obstructive lung diseases. N. Engl. J. Med. *380*, 1941-1953.

1255 Bove, P.F., Grubb, B.R., Okada, S.F., Ribeiro, C.M., Rogers, T.D., Randell, S.H.,
1256 O'Neal, W.K., and Boucher, R.C. (2010). Human alveolar type II cells secrete and
1257 absorb liquid in response to local nucleotide signaling. J. Biol. Chem. *285*, 34939-34949.

1258 Brann, D., Tsukahara, T., Weinreb, C., Logan, D.W., and Datta, S.R. (2020). Non-neural
1259 expression of SARS-CoV-2 entry genes in the olfactory epithelium suggests
1260 mechanisms underlying anosmia in COVID-19 patients. bioRxiv,
1261 http://dx.doi.org/10.1101/2020.03.25.009084.

1262 Carsana, L., Sonzogni, A., Nasr, A., Rossi, R., Pellegrinelli, A., Zerbi, P., Rech, R.,
1263 Colombo, R., Antinori, S., Corbellino, M.*, et al.* (2020). Pulmonary post-mortem findings
1264 in a large series of COVID-19 cases from Northern Italy. medRxiv,
1265 http://dx.doi.org/10.1101/2020.04.19.20054262.

1266 Casais, R., Thiel, V., Siddell, S.G., Cavanagh, D., and Britton, P. (2001). Reverse
1267 genetics system for the avian coronavirus infectious bronchitis virus. J. Virol. *75*, 12359-
1268 12369.

1269 CDC COVID-19 Response Team (2020). Preliminary estimates of the prevalence of
1270 selected underlying health conditions among patients with coronavirus disease 2019 -
1271 United States, February 12-March 28, 2020. MMWR Morb. Mortal. Wkly. Rep. *69*, 382-
1272 386.

1273 Chan, K.S., Zheng, J.P., Mok, Y.W., Li, Y.M., Liu, Y.N., Chu, C.M., and Ip, M.S. (2003).
1274 SARS: prognosis, outcome and sequelae. Respirology *8 Suppl*, S36-40.

1275 Chen, G., Sun, L., Kato, T., Okuda, K., Martino, M.B., Abzhanova, A., Lin, J.M., Gilmore,
1276 R.C., Batson, B.D., O'Neal, Y.K.*, et al.* (2019). IL-1beta dominates the promucin
1277 secretory cytokine profile in cystic fibrosis. J. Clin. Invest. *129*, 4433-4450.

1278 Cockrell, A.S., Johnson, J.C., Moore, I.N., Liu, D.X., Bock, K.W., Douglas, M.G.,
1279 Graham, R.L., Solomon, J., Torzewski, L., Bartos, C.*, et al.* (2018). A spike-modified
1280 Middle East respiratory syndrome coronavirus (MERS-CoV) infectious clone elicits mild
1281 respiratory disease in infected rhesus macaques. Sci. Rep. *8*, 10727.

1282 Colombo, C., Burgel, P.R., Gartner, S., van Koningsbruggen-Rietschel, S., Naehrlich, L.,
1283 Sermet-Gaudelus, I., and Southern, K.W. (2020). Impact of COVID-19 on people with
1284 cystic fibrosis. Lancet Respir. Med. *8*, e35-e36.

1285 Coutard, B., Valle, C., de Lamballerie, X., Canard, B., Seidah, N.G., and Decroly, E.
1286 (2020). The spike glycoprotein of the new coronavirus 2019-nCoV contains a furin-like
1287 cleavage site absent in CoV of the same clade. Antiviral Res. *176*, 104742.

1288 Deprez, M., Zaragosi, L.-E., Truchi, M., Garcia, S.R., Arguel, M.-J., Lebrigand, K.,
1289 Paquet, A., Pee'r, D., Marquette, C.-H., Leroy, S.*, et al.* (2019). A single-cell atlas of the
1290 human healthy airways. bioRxiv, http://dx.doi.org/10.1101/2019.12.21.884759.

1291 Dickson, R.P., Erb-Downward, J.R., Martinez, F.J., and Huffnagle, G.B. (2016). The
1292 microbiome and the respiratory tract. Annu. Rev. Physiol. *78*, 481-504.

1293 Durante, M.A., Kurtenbach, S., Sargi, Z.B., Harbour, J.W., Choi, R., Kurtenbach, S.,
1294 Goss, G.M., Matsunami, H., and Goldstein, B.J. (2020). Single-cell analysis of olfactory
1295 neurogenesis and differentiation in adult humans. Nat. Neurosci. *23*, 323-326.

1296 Eichner, H., Behbehani, A.A., and Hochstrasser, K. (1983). [Diagnostic value of nasal
1297 secretions, current state: normal values. 1]. Laryngol. Rhinol. Otol. (Stuttg) *62*, 561-565.

1298 Esther, C.R., Jr., Muhlebach, M.S., Ehre, C., Hill, D.B., Wolfgang, M.C., Kesimer, M.,
1299 Ramsey, K.A., Markovetz, M.R., Garbarine, I.C., Forest, M.G.*, et al.* (2019). Mucus
1300 accumulation in the lungs precedes structural changes and infection in children with
1301 cystic fibrosis. Sci. Transl. Med. *11*.

1302 Evans, C.M., Fingerlin, T.E., Schwarz, M.I., Lynch, D., Kurche, J., Warg, L., Yang, I.V.,
1303 and Schwartz, D.A. (2016). Idiopathic pulmonary fibrosis: a genetic disease that
1304 involves mucociliary dysfunction of the peripheral airways. Physiol. Rev. *96*, 1567-1591.

1305 Farzal, Z., Basu, S., Burke, A., Fasanmade, O.O., Lopez, E.M., Bennett, W.D., Ebert,
1306 C.S., Jr., Zanation, A.M., Senior, B.A., and Kimbell, J.S. (2019). Comparative study of
1307 simulated nebulized and spray particle deposition in chronic rhinosinusitis patients. Int.
1308 Forum Allergy Rhinol. *9*, 746-758.

1309 Fulcher, M.L., Gabriel, S.E., Olsen, J.C., Tatreau, J.R., Gentzsch, M., Livanos, E.,
1310 Saavedra, M.T., Salmon, P., and Randell, S.H. (2009). Novel human bronchial epithelial
1311 cell lines for cystic fibrosis research. Am. J. Physiol. Lung Cell. Mol. Physiol. *296*, L82-
1312 91.

1313 Fulcher, M.L., and Randell, S.H. (2013). Human nasal and tracheo-bronchial respiratory
1314 epithelial cell culture. Methods Mol. Biol. *945*, 109-121.

1315 Gaeckle, N.T., Pragman, A.A., Pendleton, K.M., Baldomero, A.K., and Criner, G.J.
1316 (2020). The oral-lung axis: the impact of oral health on lung health. Respir. Care,
1317 http://dx.doi.org/10.4187/respcare.07332.

1318 Gentzsch, M., Boyles, S.E., Cheluvaraju, C., Chaudhry, I.G., Quinney, N.L., Cho, C.,
1319 Dang, H., Liu, X., Schlegel, R., and Randell, S.H. (2017). Pharmacological rescue of
1320 conditionally reprogrammed cystic fibrosis bronchial epithelial cells. Am. J. Respir. Cell
1321 Mol. Biol. *56*, 568-574.

1322 Ghosh, A., Coakley, R.C., Mascenik, T., Rowell, T.R., Davis, E.S., Rogers, K., Webster,
1323 M.J., Dang, H., Herring, L.E., Sassano, M.F.*, et al.* (2018). Chronic e-cigarette exposure
1324 alters the human bronchial epithelial proteome. Am J. Respir. Crit. Care Med. *198*, 67-
1325 76.

1326 Gleeson, K., Eggli, D.F., and Maxwell, S.L. (1997). Quantitative aspiration during sleep
1327 in normal subjects. Chest *111*, 1266-1272.

1328 Gonzalez, J.M., Penzes, Z., Almazan, F., Calvo, E., and Enjuanes, L. (2002).
1329 Stabilization of a full-length infectious cDNA clone of transmissible gastroenteritis
1330 coronavirus by insertion of an intron. J. Virol. *76*, 4655-4661.

1331 Gorbalenya, A.E., Baker, S.C., Baric, R.S., de Groot, R.J., Drosten, C., Gulyaeva, A.A.,
1332 Haagmans, B.L., Lauber, C., Leontovich, A.M., Neuman, B.W*., et al.* (2020). The
1333 species Severe acute respiratory syndrome-related coronavirus: classifying 2019-nCoV
1334 and naming it SARS-CoV-2. Nat. Microbiol. *5*, 536-544.

1335 Guan, W.J., Liang, W.H., Zhao, Y., Liang, H.R., Chen, Z.S., Li, Y.M., Liu, X.Q., Chen,
1336 R.C., Tang, C.L., Wang, T*., et al.* (2020). Comorbidity and its impact on 1590 patients
1337 with Covid-19 in China: a nationwide analysis. Eur. Respir. J.,
1338 http://dx.doi.org/10.1183/13993003.00547-2020.

1339 Hoffmann, M., Kleine-Weber, H., Schroeder, S., Kruger, N., Herrler, T., Erichsen, S.,
1340 Schiergens, T.S., Herrler, G., Wu, N.H., Nitsche, A*., et al.* (2020). SARS-CoV-2 cell
1341 entry depends on ACE2 and TMPRSS2 and is blocked by a clinically proven protease
1342 inhibitor. Cell *181*, 271-280.e278.

1343 Huang, C., Wang, Y., Li, X., Ren, L., Zhao, J., Hu, Y., Zhang, L., Fan, G., Xu, J., Gu, X.,
1344 *et al.* (2020). Clinical features of patients infected with 2019 novel coronavirus in Wuhan,
1345 China. Lancet *395*, 497-506.

1346 Huxley, E.J., Viroslav, J., Gray, W.R., and Pierce, A.K. (1978). Pharyngeal aspiration in
1347 normal adults and patients with depressed consciousness. Am. J. Med. *64*, 564-568.

1348 Imai, Y., Kuba, K., Rao, S., Huan, Y., Guo, F., Guan, B., Yang, P., Sarao, R., Wada, T.,
1349 Leong-Poi, H*., et al.* (2005). Angiotensin-converting enzyme 2 protects from severe
1350 acute lung failure. Nature *436*, 112-116.

1351 Izaguirre, G. (2019). The proteolytic regulation of virus cell entry by furin and other
1352 proprotein convertases. Viruses *11*.

1353 Jia, H. (2016). Pulmonary angiotensin-converting enzyme 2 (ACE2) and inflammatory
1354 lung disease. Shock *46*, 239-248.

1355 Keeler, S.P., Agapov, E.V., Hinojosa, M.E., Letvin, A.N., Wu, K., and Holtzman, M.J.
1356 (2018). Influenza A virus infection causes chronic lung disease linked to sites of active
1357 viral RNA remnants. J. Immunol. *201*, 2354-2368.

1358 Kesic, M.J., Simmons, S.O., Bauer, R., and Jaspers, I. (2011). Nrf2 expression modifies
1359 influenza A entry and replication in nasal epithelial cells. Free Radic. Biol. Med. *51*, 444-
1360 453.

1361 Knowles, M.R., Ostrowski, L.E., Leigh, M.W., Sears, P.R., Davis, S.D., Wolf, W.E.,
1362 Hazucha, M.J., Carson, J.L., Olivier, K.N., Sagel, S.D*., et al.* (2014). Mutations in
1363 RSPH1 cause primary ciliary dyskinesia with a unique clinical and ciliary phenotype. Am
1364 J. Respir. Crit. Care Med. *189*, 707-717.

Kollias, A., Kyriakoulis, K.G., Dimakakos, E., Poulakou, G., Stergiou, G.S., and Syrigos, K. (2020). Thromboembolic risk and anticoagulant therapy in COVID-19 patients: emerging evidence and call for action. Br. J. Haematol., http://dx.doi.org/10.1111/bjh.16727.

Kuba, K., Imai, Y., Rao, S., Gao, H., Guo, F., Guan, B., Huan, Y., Yang, P., Zhang, Y., Deng, W.*, et al.* (2005). A crucial role of angiotensin converting enzyme 2 (ACE2) in SARS coronavirus-induced lung injury. Nat. Med. *11*, 875-879.

Kuznetsova, A., Brockhoff, P.B., and Christensen, R.H.B. (2017). lmerTest package: tests in linear mixed effects models. J. Stat. Softw. *82*, 1-26.

Leung, J.M., Yang, C.X., Tam, A., Shaipanich, T., Hackett, T.L., Singhera, G.K., Dorscheid, D.R., and Sin, D.D. (2020). ACE-2 expression in the small airway epithelia of smokers and COPD patients: implications for COVID-19. Eur. Respir. J., http://dx.doi.org/10.1183/13993003.00688-2020.

Liu, Y., Ning, Z., Chen, Y., Guo, M., Liu, Y., Gali, N.K., Sun, L., Duan, Y., Cai, J., Westerdahl, D.*, et al.* (2020). Aerodynamic analysis of SARS-CoV-2 in two Wuhan hospitals. Nature, http://dx.doi.org/10.1038/s41586-020-2271-3.

Magro, C., Mulvey, J.J., Berlin, D., Nuovo, G., Salvatore, S., Harp, J., Baxter-Stoltzfus, A., and Laurence, J. (2020). Complement associated microvascular injury and thrombosis in the pathogenesis of severe COVID-19 infection: a report of five cases. Transl. Res., http://dx.doi.org/10.1016/j.trsl.2020.04.007.

Martinez, D.R., Tu, J.J., Kumar, A., Mangold, J.F., Mangan, R.J., Goswami, R., Giorgi, E.E., Chen, J., Mengual, M., Douglas, A.O.*, et al.* (2020). Maternal broadly neutralizing antibodies can select for neutralization-resistant, infant-transmitted/founder HIV variants. mBio *11*.

Matsuyama, S., Nagata, N., Shirato, K., Kawase, M., Takeda, M., and Taguchi, F. (2010). Efficient activation of the severe acute respiratory syndrome coronavirus spike protein by the transmembrane protease TMPRSS2. J. Virol. *84*, 12658-12664.

Matsuyama, S., Ujike, M., Morikawa, S., Tashiro, M., and Taguchi, F. (2005). Protease-mediated enhancement of severe acute respiratory syndrome coronavirus infection. Proc. Natl. Acad. Sci. U.S.A. *102*, 12543-12547.

Menachery, V.D., Dinnon, K.H., 3rd, Yount, B.L., Jr., McAnarney, E.T., Gralinski, L.E., Hale, A., Graham, R.L., Scobey, T., Anthony, S.J., Wang, L.*, et al.* (2020). Trypsin treatment unlocks barrier for zoonotic bat coronavirus infection. J. Virol. *94*.

Menachery, V.D., Eisfeld, A.J., Schafer, A., Josset, L., Sims, A.C., Proll, S., Fan, S., Li, C., Neumann, G., Tilton, S.C.*, et al.* (2014). Pathogenic influenza viruses and coronaviruses utilize similar and contrasting approaches to control interferon-stimulated gene responses. mBio *5*, e01174-01114.

1402 Menachery, V.D., Yount, B.L., Jr., Debbink, K., Agnihothram, S., Gralinski, L.E., Plante,
1403 J.A., Graham, R.L., Scobey, T., Ge, X.Y., Donaldson, E.F*., et al.* (2015). A SARS-like
1404 cluster of circulating bat coronaviruses shows potential for human emergence. Nat. Med.
1405 *21*, 1508-1513.

1406 Millet, J.K., and Whittaker, G.R. (2014). Host cell entry of Middle East respiratory
1407 syndrome coronavirus after two-step, furin-mediated activation of the spike protein. Proc.
1408 Natl. Acad. Sci. U.S.A. *111*, 15214-15219.

1409 Morawska, L., and Cao, J. (2020). Airborne transmission of SARS-CoV-2: the world
1410 should face the reality. Environ. Int. *139*, 105730.

1411 Mossel, E.C., Wang, J., Jeffers, S., Edeen, K.E., Wang, S., Cosgrove, G.P., Funk, C.J.,
1412 Manzer, R., Miura, T.A., Pearson, L.D*., et al.* (2008). SARS-CoV replicates in primary
1413 human alveolar type II cell cultures but not in type I-like cells. Virology *372*, 127-135.

1414 Odani, K., Tachibana, M., Tamashima, R., and Tsutsumi, Y. (2019). Herpes simplex
1415 virus pneumonia: importance of aspiration etiology. Case Rep. Pathol. *2019*, 7623576.

1416 Okuda, K., Chen, G., Subramani, D.B., Wolf, M., Gilmore, R.C., Kato, T., Radicioni, G.,
1417 Kesimer, M., Chua, M., Dang, H*., et al.* (2019). Localization of secretory mucins
1418 MUC5AC and MUC5B in normal/healthy human airways. Am J. Respir. Crit. Care Med.
1419 *199*, 715-727.

1420 Ota, C., Ng-Blichfeldt, J.P., Korfei, M., Alsafadi, H.N., Lehmann, M., Skronska-Wasek,
1421 W., M, M.D.S., Guenther, A., Wagner, D.E., and Konigshoff, M. (2018). Dynamic
1422 expression of HOPX in alveolar epithelial cells reflects injury and repair during the
1423 progression of pulmonary fibrosis. Sci Rep *8*, 12983.

1424 Pan, X., Chen, D., Xia, Y., Wu, X., Li, T., Ou, X., Zhou, L., and Liu, J. (2020a).
1425 Asymptomatic cases in a family cluster with SARS-CoV-2 infection. Lancet Infect. Dis.
1426 *20*, 410-411.

1427 Pan, Y., Zhang, D., Yang, P., Poon, L.L.M., and Wang, Q. (2020b). Viral load of SARS-
1428 CoV-2 in clinical samples. Lancet Infect. Dis. *20*, 411-412.

1429 Pandya, V.K., and Tiwari, R.S. (2006). Nasal mucociliary clearance in health and
1430 disease. Indian J. Otolaryngol. Head Neck Surg. *58*, 332-334.

1431 Papineni, R.S., and Rosenthal, F.S. (1997). The size distribution of droplets in the
1432 exhaled breath of healthy human subjects. J. Aerosol Med. *10*, 105-116.

1433 Phillips, L.K., Deane, A.M., Jones, K.L., Rayner, C.K., and Horowitz, M. (2015). Gastric
1434 emptying and glycaemia in health and diabetes mellitus. Nat. Rev. Endocrinol. *11*, 112-
1435 128.

1436 Quirouette, C., Younis, N.P., Reddy, M.B., and Beauchemin, C.A.A. (2020). A
1437 mathematical model describing the localization and spread of influenza A virus infection
1438 within the human respiratory tract. PLoS Comput. Biol. *16*, e1007705.

1439 Richard, M., van den Brand, J.M.A., Bestebroer, T.M., Lexmond, P., de Meulder, D.,
1440 Fouchier, R.A.M., Lowen, A.C., and Herfst, S. (2020). Influenza A viruses are
1441 transmitted via the air from the nasal respiratory epithelium of ferrets. Nat. Commun. *11*,
1442 766.

1443 Rockx, B., Kuiken, T., Herfst, S., Bestebroer, T., Lamers, M.M., Oude Munnink, B.B., de
1444 Meulder, D., van Amerongen, G., van den Brand, J., Okba, N.M.A*., et al.* (2020).
1445 Comparative pathogenesis of COVID-19, MERS, and SARS in a nonhuman primate
1446 model. Science, http://dx.doi.org/10.1126/science.abb7314.

1447 Rogers, A.J., Solus, J.F., Hunninghake, G.M., Baron, R.M., Meyer, N.J., Janz, D.R.,
1448 Schwartz, D.A., May, A.K., Lawson, W.E., Blackwell, T.S*., et al.* (2018). MUC5B
1449 promoter polymorphism and development of acute respiratory distress syndrome. Am J.
1450 Respir. Crit. Care Med. *198*, 1342-1345.

1451 Sajuthi, S.P., DeFord, P., Jackson, N.D., Montgomery, M.T., Everman, J.L., Rios, C.L.,
1452 Pruesse, E., Nolin, J.D., Plender, E.G., Wechsler, M.E*., et al.* (2020). Type 2 and
1453 interferon inflammation strongly regulate SARS-CoV-2 related gene expression in the
1454 airway epithelium. bioRxiv, http://dx.doi.org/10.1101/2020.04.09.034454.

1455 Santarpia, J.L., Rivera, D.N., Herrera, V., Morwitzer, M.J., Creager, H., Santarpia, G.W.,
1456 Crown, K.K., Brett-Major, D., Schnaubelt, E., Broadhurst, M.J*., et al.* (2020).
1457 Transmission potential of SARS-CoV-2 in viral shedding observed at the University of
1458 Nebraska Medical Center. medRxiv, http://dx.doi.org/10.1101/2020.03.23.20039446.

1459 Schindelin, J., Arganda-Carreras, I., Frise, E., Kaynig, V., Longair, M., Pietzsch, T.,
1460 Preibisch, S., Rueden, C., Saalfeld, S., Schmid, B*., et al.* (2012). Fiji: an open-source
1461 platform for biological-image analysis. Nat. Methods *9*, 676-682.

1462 Scobey, T., Yount, B.L., Sims, A.C., Donaldson, E.F., Agnihothram, S.S., Menachery,
1463 V.D., Graham, R.L., Swanstrom, J., Bove, P.F., Kim, J.D*., et al.* (2013). Reverse
1464 genetics with a full-length infectious cDNA of the Middle East respiratory syndrome
1465 coronavirus. Proc. Natl. Acad. Sci. U.S.A. *110*, 16157-16162.

1466 Shang, J., Ye, G., Shi, K., Wan, Y., Luo, C., Aihara, H., Geng, Q., Auerbach, A., and Li,
1467 F. (2020). Structural basis of receptor recognition by SARS-CoV-2. Nature,
1468 http://dx.doi.org/10.1038/s41586-020-2179-y.

1469 Sims, A.C., Baric, R.S., Yount, B., Burkett, S.E., Collins, P.L., and Pickles, R.J. (2005).
1470 Severe acute respiratory syndrome coronavirus infection of human ciliated airway
1471 epithelia: role of ciliated cells in viral spread in the conducting airways of the lungs. J.
1472 Virol. *79*, 15511-15524.

1473 Sodhi, C.P., Nguyen, J., Yamaguchi, Y., Werts, A.D., Lu, P., Ladd, M.R., Fulton, W.B.,
1474 Kovler, M.L., Wang, S., Prindle, T., Jr*., et al.* (2019). A dynamic variation of pulmonary
1475 ACE2 is required to modulate neutrophilic inflammation in response to Pseudomonas
1476 aeruginosa lung infection in mice. J. Immunol. *203*, 3000-3012.

1477 Speen, A.M., Hoffman, J.R., Kim, H.H., Escobar, Y.N., Nipp, G.E., Rebuli, M.E., Porter,
1478 N.A., and Jaspers, I. (2019). Small molecule antipsychotic aripiprazole potentiates
1479 ozone-induced inflammation in airway epithelium. Chem. Res. Toxicol. *32*, 1997-2005.

1480 Sungnak, W., Huang, N., Becavin, C., Berg, M., Queen, R., Litvinukova, M., Talavera-
1481 Lopez, C., Maatz, H., Reichart, D., Sampaziotis, F*., et al.* (2020). SARS-CoV-2 entry
1482 factors are highly expressed in nasal epithelial cells together with innate immune genes.
1483 Nat. Med., http://dx.doi.org/10.1038/s41591-020-0868-6.

1484 Teunis, P.F., Brienen, N., and Kretzschmar, M.E. (2010). High infectivity and
1485 pathogenicity of influenza A virus via aerosol and droplet transmission. Epidemics *2*,
1486 215-222.

1487 Thao, T.T.N., Labroussaa, F., Ebert, N., V'Kovski, P., Stalder, H., Portmann, J., Kelly, J.,
1488 Steiner, S., Holwerda, M., Kratzel, A*., et al.* (2020). Rapid reconstruction of SARS-CoV-
1489 2 using a synthetic genomics platform. Nature, http://dx.doi.org/10.1038/s41586-020-
1490 2294-9.

1491 Thornton, D.J., Gray, T., Nettesheim, P., Howard, M., Koo, J.S., and Sheehan, J.K.
1492 (2000). Characterization of mucins from cultured normal human tracheobronchial
1493 epithelial cells. Am. J. Physiol. Lung Cell. Mol. Physiol. *278*, L1118-1128.

1494 Tian, X., Li, C., Huang, A., Xia, S., Lu, S., Shi, Z., Lu, L., Jiang, S., Yang, Z., Wu, Y*., et*
1495 *al.* (2020). Potent binding of 2019 novel coronavirus spike protein by a SARS
1496 coronavirus-specific human monoclonal antibody. Emerg. Microbes Infect. *9*, 382-385.

1497 Walls, A.C., Park, Y.J., Tortorici, M.A., Wall, A., McGuire, A.T., and Veesler, D. (2020).
1498 Structure, function, and antigenicity of the SARS-CoV-2 spike glycoprotein. Cell *181*,
1499 281-292.e286.

1500 Wang, N., Rosen, O., Wang, L., Turner, H.L., Stevens, L.J., Corbett, K.S., Bowman,
1501 C.A., Pallesen, J., Shi, W., Zhang, Y*., et al.* (2019). Structural definition of a
1502 neutralization-sensitive epitope on the MERS-CoV S1-NTD. Cell Rep. *28*, 3395-
1503 3405.e3396.

1504 Wicht, O., Li, W., Willems, L., Meuleman, T.J., Wubbolts, R.W., van Kuppeveld, F.J.,
1505 Rottier, P.J., and Bosch, B.J. (2014). Proteolytic activation of the porcine epidemic
1506 diarrhea coronavirus spike fusion protein by trypsin in cell culture. J. Virol. *88*, 7952-
1507 7961.

1508 Wilson, N.M., Norton, A., Young, F.P., and Collins, D.W. (2020). Airborne transmission
1509 of severe acute respiratory syndrome coronavirus-2 to healthcare workers: a narrative
1510 review. Anaesthesia, http://dx.doi.org/10.1111/anae.15093.

1511 Wölfel, R., Corman, V.M., Guggemos, W., Seilmaier, M., Zange, S., Muller, M.A.,
1512 Niemeyer, D., Jones, T.C., Vollmar, P., Rothe, C.*, et al.* (2020). Virological assessment
1513 of hospitalized patients with COVID-2019. Nature, http://dx.doi.org/10.1038/s41586-
1514 020-2196-x.

1515 Wrapp, D., Wang, N., Corbett, K.S., Goldsmith, J.A., Hsieh, C.L., Abiona, O., Graham,
1516 B.S., and McLellan, J.S. (2020). Cryo-EM structure of the 2019-nCoV spike in the
1517 prefusion conformation. Science *367*, 1260-1263.

1518 Wu, A., Peng, Y., Huang, B., Ding, X., Wang, X., Niu, P., Meng, J., Zhu, Z., Zhang, Z.,
1519 Wang, J.*, et al.* (2020a). Genome composition and divergence of the novel coronavirus
1520 (2019-nCoV) originating in China. Cell Host Microbe *27*, 325-328.

1521 Wu, X., Nethery, R.C., Sabath, B.M., Braun, D., and Dominici, F. (2020b). Exposure to
1522 air pollution and COVID-19 mortality in the United States. medRxiv,
1523 http://dx.doi.org/10.1101/2020.04.05.20054502.

1524 Wu, Z., and McGoogan, J.M. (2020). Characteristics of and important lessons from the
1525 coronavirus disease 2019 (COVID-19) outbreak in China: summary of a report of 72314
1526 cases from the Chinese Center for Disease Control and Prevention. JAMA,
1527 http://dx.doi.org/10.1001/jama.2020.2648.

1528 Xie, X., Muruato, A., Lokugamage, K.G., Narayanan, K., Zhang, X., Zou, J., Liu, J.,
1529 Schindewolf, C., Bopp, N.E., Aguilar, P.V.*, et al.* (2020). An infectious cDNA clone of
1530 SARS-CoV-2. Cell Host Microbe, http://dx.doi.org/10.1016/j.chom.2020.04.004.

1531 Xu, X., Yu, C., Qu, J., Zhang, L., Jiang, S., Huang, D., Chen, B., Zhang, Z., Guan, W.,
1532 Ling, Z.*, et al.* (2020). Imaging and clinical features of patients with 2019 novel
1533 coronavirus SARS-CoV-2. Eur. J. Nucl. Med. Mol. Imaging *47*, 1275-1280.

1534 Yan, R., Zhang, Y., Li, Y., Xia, L., Guo, Y., and Zhou, Q. (2020). Structural basis for the
1535 recognition of SARS-CoV-2 by full-length human ACE2. Science *367*, 1444-1448.

1536 Ying, T., Prabakaran, P., Du, L., Shi, W., Feng, Y., Wang, Y., Wang, L., Li, W., Jiang, S.,
1537 Dimitrov, D.S.*, et al.* (2015). Junctional and allele-specific residues are critical for
1538 MERS-CoV neutralization by an exceptionally potent germline-like antibody. Nat.
1539 Commun. *6*, 8223.

1540 Yount, B., Curtis, K.M., and Baric, R.S. (2000). Strategy for systematic assembly of
1541 large RNA and DNA genomes: transmissible gastroenteritis virus model. J. Virol. *74*,
1542 10600-10611.

1543 Yount, B., Curtis, K.M., Fritz, E.A., Hensley, L.E., Jahrling, P.B., Prentice, E., Denison,
1544 M.R., Geisbert, T.W., and Baric, R.S. (2003). Reverse genetics with a full-length
1545 infectious cDNA of severe acute respiratory syndrome coronavirus. Proc. Natl. Acad.
1546 Sci. U.S.A. *100*, 12995-13000.

Yu, X., Zhang, S., Jiang, L., Cui, Y., Li, D., Wang, D., Wang, N., Fu, L., Shi, X., Li, Z.*, et al.* (2015). Structural basis for the neutralization of MERS-CoV by a human monoclonal antibody MERS-27. Sci. Rep. *5*, 13133.

Zhu, N., Zhang, D., Wang, W., Li, X., Yang, B., Song, J., Zhao, X., Huang, B., Shi, W., Lu, R.*, et al.* (2020). A novel coronavirus from patients with pneumonia in China, 2019. N. Engl. J. Med. *382*, 727-733.

Zhu, Z., Chakraborti, S., He, Y., Roberts, A., Sheahan, T., Xiao, X., Hensley, L.E., Prabakaran, P., Rockx, B., Sidorov, I.A.*, et al.* (2007). Potent cross-reactive neutralization of SARS coronavirus isolates by human monoclonal antibodies. Proc. Natl. Acad. Sci. U.S.A. *104*, 12123-12128.

Zou, L., Ruan, F., Huang, M., Liang, L., Huang, H., Hong, Z., Yu, J., Kang, M., Song, Y., Xia, J.*, et al.* (2020). SARS-CoV-2 viral load in upper respiratory specimens of infected patients. N. Engl. J. Med. *382*, 1177-1179.

Highlights:

1. A SARS-CoV-2 infectious cDNA clone and reporter viruses are generated.
2. SARS-CoV-2 and SARS-CoV neutralization assays shows limited cross neutralization.
3. SARS-CoV-2 shows a gradient infectivity from the proximal to distal respiratory tract.
4. Ciliated airway cells and AT-2 cells are primary targets for SARS-CoV-2 infection.

In Brief

Hou et al. present a reverse genetics system for SARS-CoV-2, which is then used to make reporter viruses to quantify the ability of patient sera and antibodies to neutralize infectious virus and to examine viral tropism along the human respiratory tract.

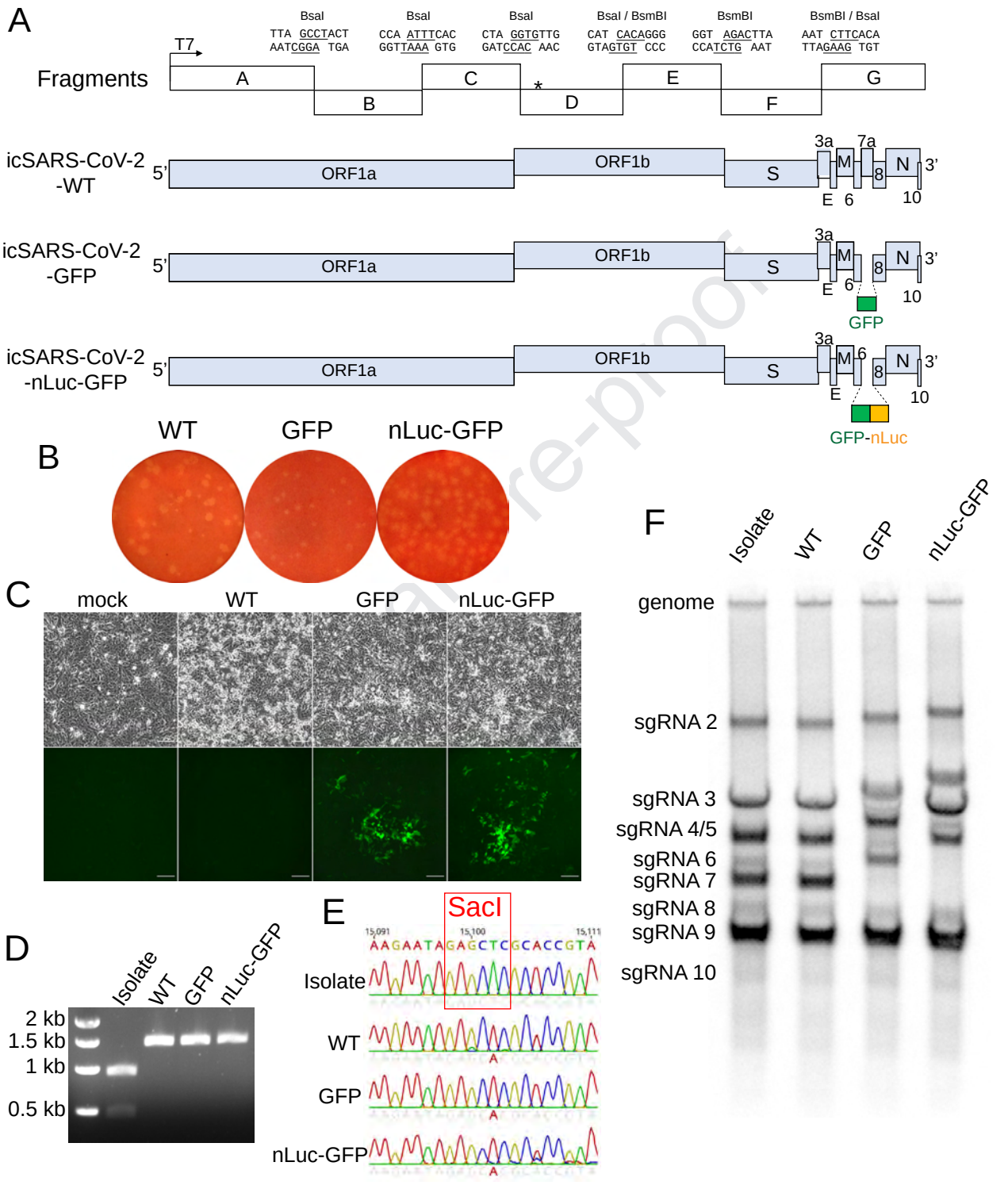
A
BsaI
TTA GCCTACT
AATCGGA TGA
BsaI
CCA ATTTCAC
GGTTAAA GTG
BsaI
CTA GGTGTTG
GATCCAC AAC
BsaI / BsmBI
CAT CACAGGG
GTAGTGT CCC
BsmBI
GGT AGACTTA
CCATCTG AAT
BsmBI / BsaI
AAT CTTCACA
TTAGAAG TGT
T7
Fragments
A
B
C
D
E
F
G
icSARS-CoV-2
-WT
icSARS-CoV-2
-GFP
icSARS-CoV-2
-nLuc-GFP
5'
ORF1a
ORF1b
S
3a
M
7a
N
3'
E
6
8
10
GFP
GFP-nLuc
B
WT
GFP
nLuc-GFP
C
mock
WT
GFP
nLuc-GFP
D
Isolate
WT
GFP
nLuc-GFP
2 kb
1.5 kb
1 kb
0.5 kb
E
SacI
15,091
15,100
15,111
AAGAATAGAGCTCGCACCGTA
Isolate
WT
GFP
nLuc-GFP
F
Isolate
WT
GFP
nLuc-GFP
genome
sgRNA 2
sgRNA 3
sgRNA 4/5
sgRNA 6
sgRNA 7
sgRNA 8
sgRNA 9
sgRNA 10

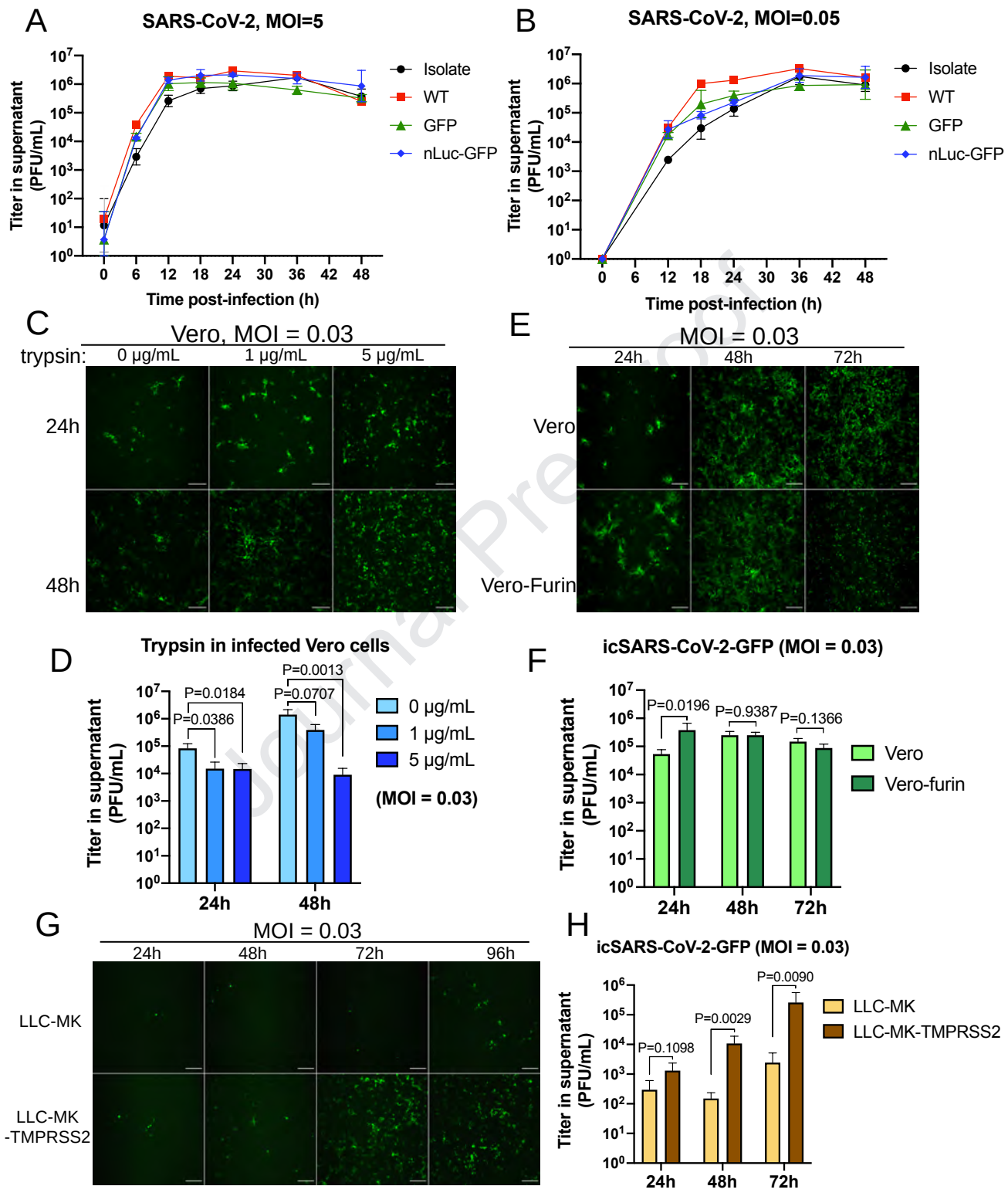
A
SARS-CoV-2, MOI=5
Titer in supernatant (PFU/mL)
Time post-infection (h)
Isolate
WT
GFP
nLuc-GFP
B
SARS-CoV-2, MOI=0.05
Titer in supernatant (PFU/mL)
Time post-infection (h)
Isolate
WT
GFP
nLuc-GFP
C
Vero, MOI = 0.03
trypsin:
0 μg/mL
1 μg/mL
5 μg/mL
24h
48h
E
MOI = 0.03
24h
48h
72h
Vero
Vero-Furin
D
Trypsin in infected Vero cells
Titer in supernatant (PFU/mL)
P=0.0184
P=0.0386
P=0.0013
P=0.0707
0 μg/mL
1 μg/mL
5 μg/mL
(MOI = 0.03)
24h
48h
F
icSARS-CoV-2-GFP (MOI = 0.03)
Titer in supernatant (PFU/mL)
P=0.0196
P=0.9387
P=0.1366
Vero
Vero-furin
24h
48h
72h
G
MOI = 0.03
24h
48h
72h
96h
LLC-MK
LLC-MK -TMPRSS2
H
icSARS-CoV-2-GFP (MOI = 0.03)
Titer in supernatant (PFU/mL)
P=0.1098
P=0.0029
P=0.0090
LLC-MK
LLC-MK-TMPRSS2
24h
48h
72h

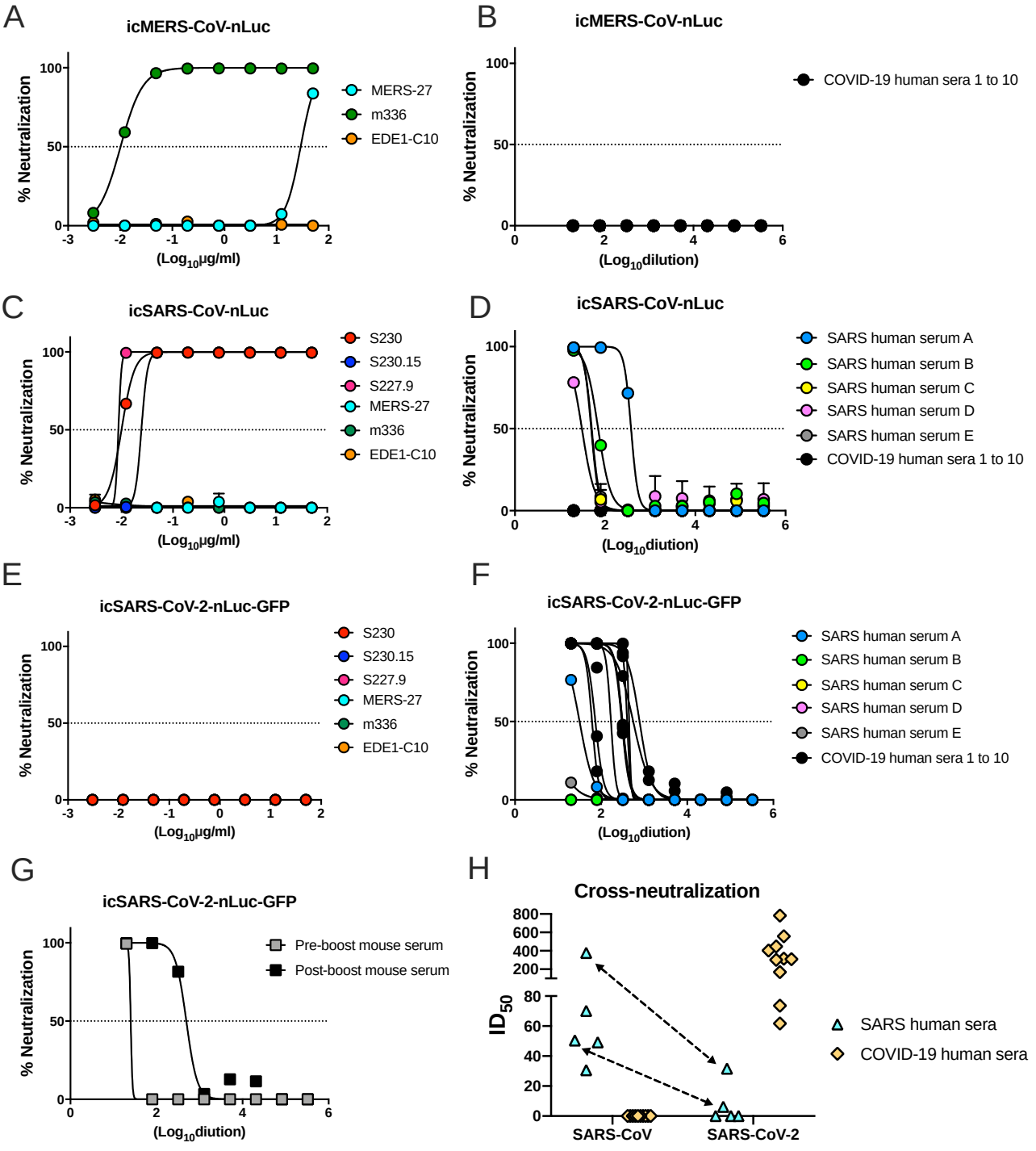
A
icMERS-CoV-nLuc
% Neutralization
(Log10µg/ml)
MERS-27
m336
EDE1-C10
B
icMERS-CoV-nLuc
% Neutralization
(Log10dilution)
COVID-19 human sera 1 to 10
C
icSARS-CoV-nLuc
% Neutralization
(Log10µg/ml)
S230
S230.15
S227.9
MERS-27
m336
EDE1-C10
D
icSARS-CoV-nLuc
% Neutralization
(Log10diution)
SARS human serum A
SARS human serum B
SARS human serum C
SARS human serum D
SARS human serum E
COVID-19 human sera 1 to 10
E
icSARS-CoV-2-nLuc-GFP
% Neutralization
(Log10µg/ml)
S230
S230.15
S227.9
MERS-27
m336
EDE1-C10
F
icSARS-CoV-2-nLuc-GFP
% Neutralization
(Log10diution)
SARS human serum A
SARS human serum B
SARS human serum C
SARS human serum D
SARS human serum E
COVID-19 human sera 1 to 10
G
icSARS-CoV-2-nLuc-GFP
% Neutralization
(Log10diution)
Pre-boost mouse serum
Post-boost mouse serum
H
Cross-neutralization
ID50
SARS-CoV
SARS-CoV-2
SARS human sera
COVID-19 human sera

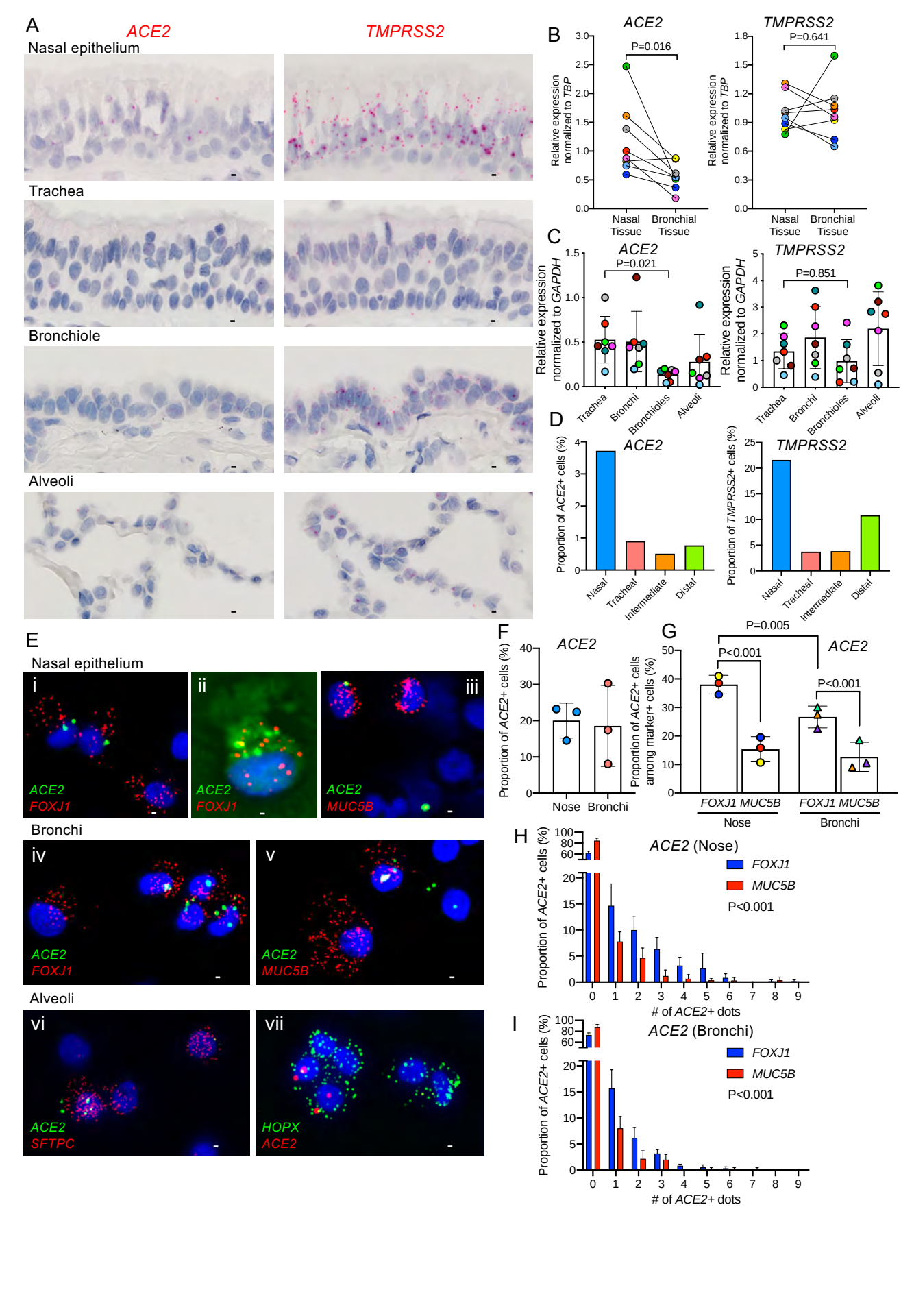
A
ACE2
TMPRSS2
Nasal epithelium
Trachea
Bronchiole
Alveoli
B
ACE2
TMPRSS2
P=0.016
P=0.641
Relative expression normalized to TBP
Nasal Tissue
Bronchial Tissue
C
ACE2
TMPRSS2
P=0.021
P=0.851
Relative expression normalized to GAPDH
Trachea
Bronchi
Bronchioles
Alveoli
D
ACE2
TMPRSS2
Proportion of ACE2+ cells (%)
Proportion of TMPRSS2+ cells (%)
Nasal
Tracheal
Intermediate
Distal
E
Nasal epithelium
i
ii
iii
ACE2
FOXJ1
ACE2
FOXJ1
ACE2
MUC5B
Bronchi
iv
v
ACE2
FOXJ1
ACE2
MUC5B
Alveoli
vi
vii
ACE2
SFTPC
HOPX
ACE2
F
ACE2
Proportion of ACE2+ cells (%)
Nose
Bronchi
G
ACE2
P=0.005
P<0.001
P<0.001
Proportion of ACE2+ cells among marker+ cells (%)
FOXJ1 MUC5B
FOXJ1 MUC5B
Nose
Bronchi
H
ACE2 (Nose)
FOXJ1
MUC5B
P<0.001
Proportion of ACE2+ cells (%)
# of ACE2+ dots
I
ACE2 (Bronchi)
FOXJ1
MUC5B
P<0.001
Proportion of ACE2+ cells (%)
# of ACE2+ dots

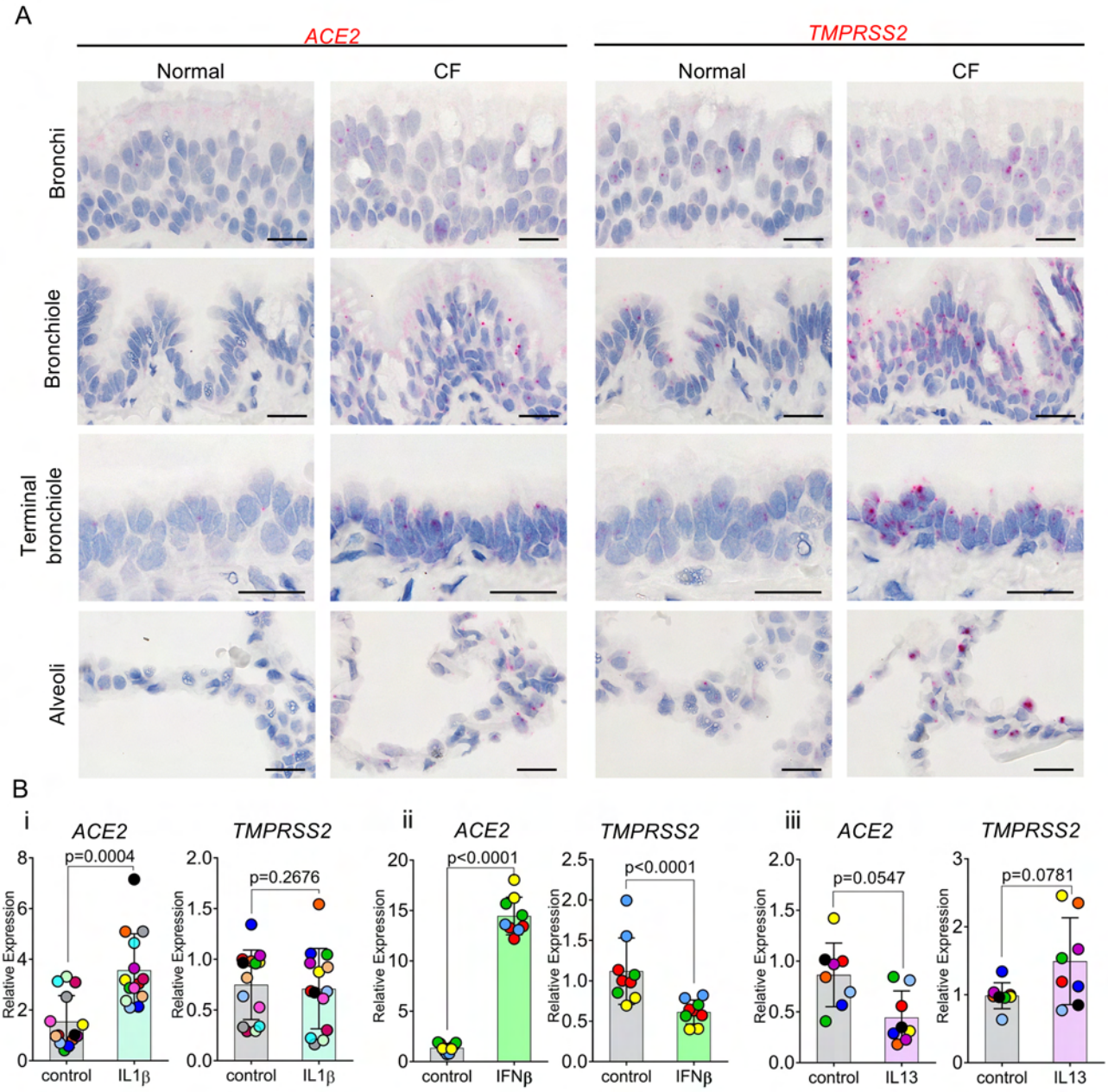
A
ACE2
TMPRSS2
Normal
CF
Normal
CF
Bronchi
Bronchiole
Terminal bronchiole
Alveoli
B
i
ACE2
p=0.0004
Relative Expression
control
IL1β
TMPRSS2
p=0.2676
control
IL1β
ii
ACE2
p<0.0001
control
IFNβ
TMPRSS2
p<0.0001
control
IFNβ
iii
ACE2
p=0.0547
control
IL13
TMPRSS2
p=0.0781
control
IL13

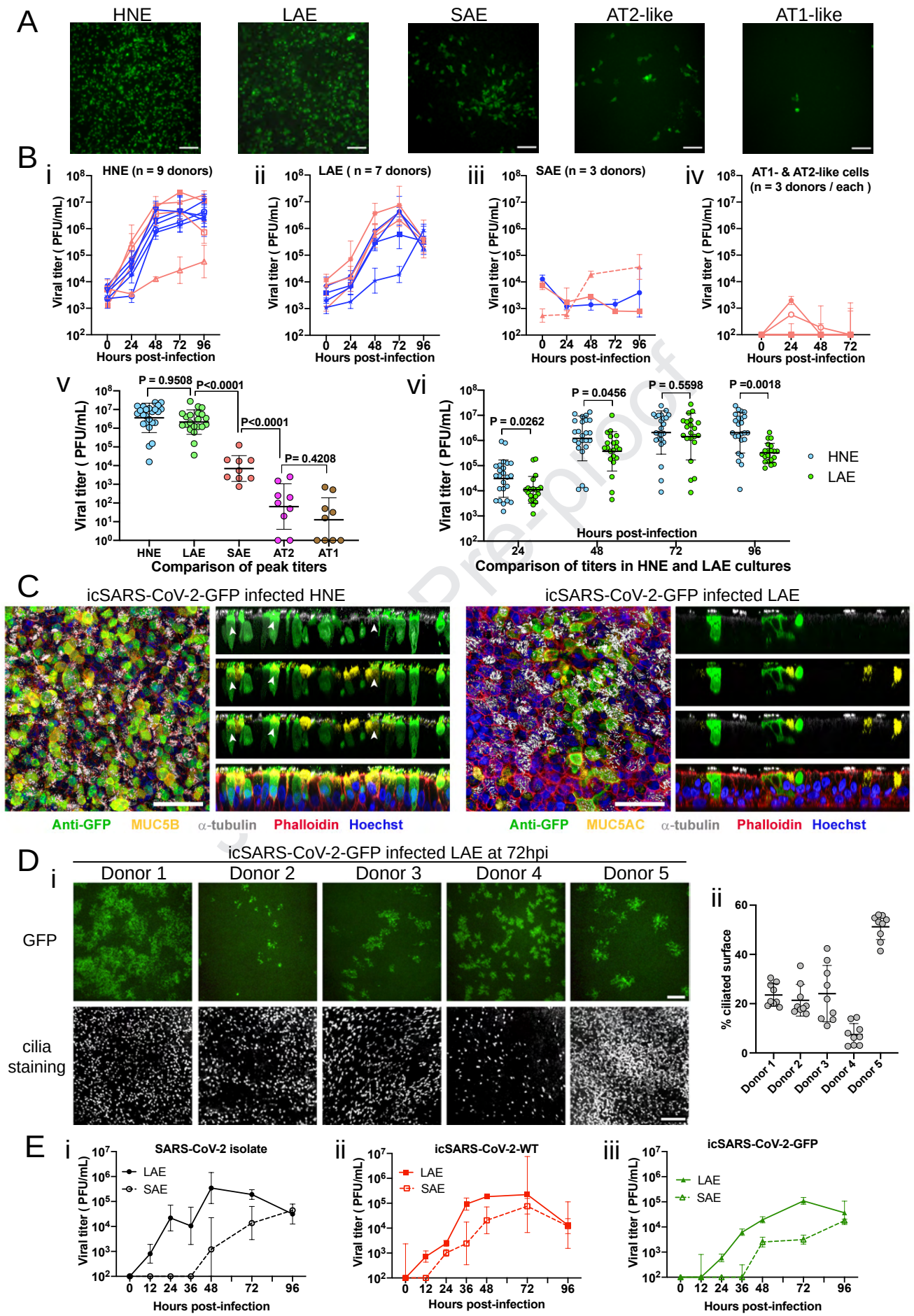
A
HNE
LAE
SAE
AT2-like
AT1-like
B
i
HNE (n = 9 donors)
ii
LAE (n = 7 donors)
iii
SAE (n = 3 donors)
iv
AT1- & AT2-like cells
(n = 3 donors / each)
Viral titer (PFU/mL)
Hours post-infection
v
P = 0.9508
P<0.0001
P<0.0001
P= 0.4208
HNE
LAE
SAE
AT2
AT1
Comparison of peak titers
vi
P = 0.0262
P = 0.0456
P = 0.5598
P =0.0018
HNE
LAE
Hours post-infection
Comparison of titers in HNE and LAE cultures
C
icSARS-CoV-2-GFP infected HNE
icSARS-CoV-2-GFP infected LAE
Anti-GFP
MUC5B
α-tubulin
Phalloidin
Hoechst
Anti-GFP
MUC5AC
α-tubulin
Phalloidin
Hoechst
D
i
icSARS-CoV-2-GFP infected LAE at 72hpi
Donor 1
Donor 2
Donor 3
Donor 4
Donor 5
GFP
cilia staining
ii
% ciliated surface
Donor 1
Donor 2
Donor 3
Donor 4
Donor 5
E
i
SARS-CoV-2 isolate
ii
icSARS-CoV-2-WT
iii
icSARS-CoV-2-GFP
LAE
SAE
Viral titer (PFU/mL)
Hours post-infection

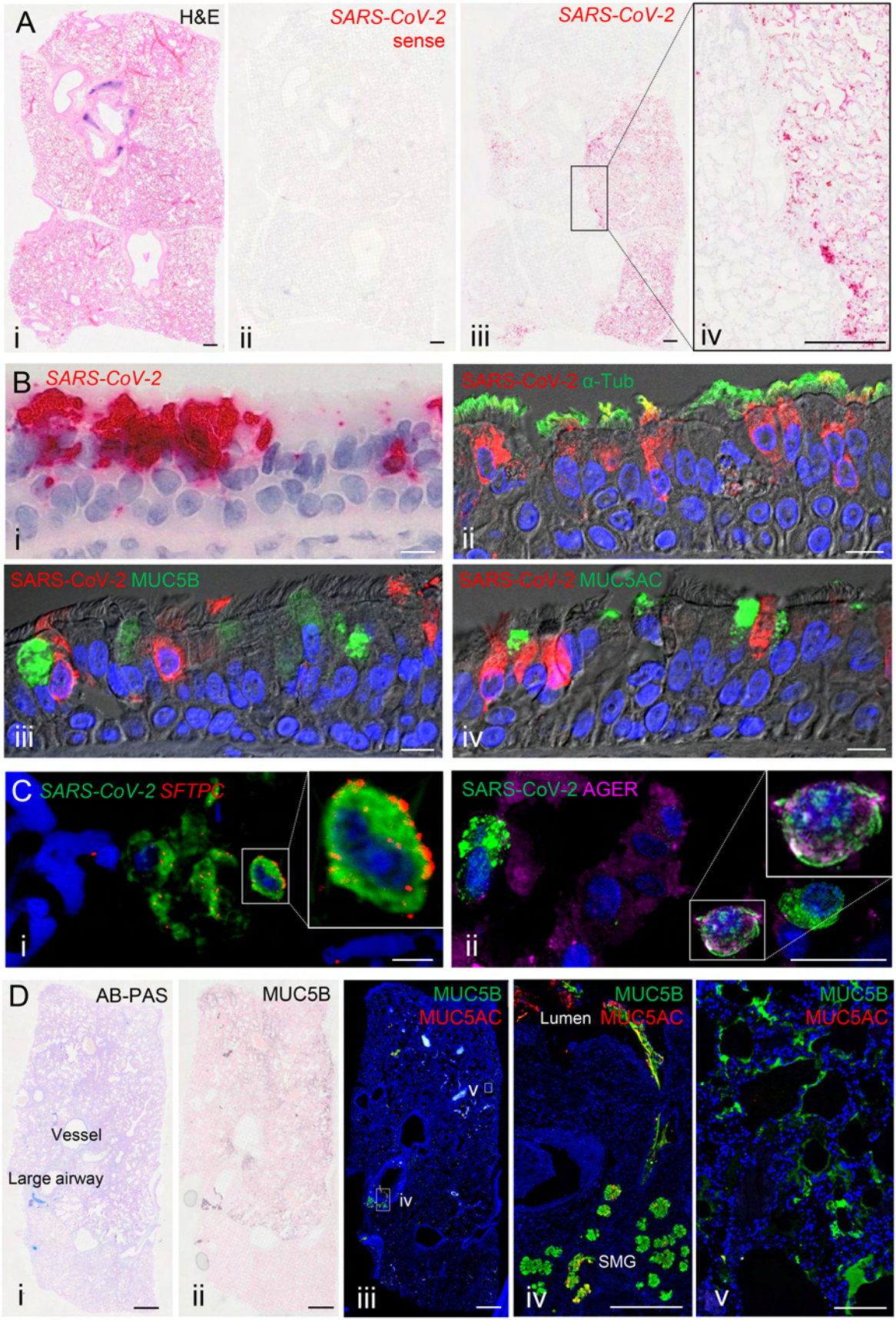
A
H&E
i
SARS-CoV-2
sense
ii
SARS-CoV-2
iii
iv
B
SARS-CoV-2
i
SARS-CoV-2 α-Tub
ii
SARS-CoV-2 MUC5B
iii
SARS-CoV-2 MUC5AC
iv
C
SARS-CoV-2 SFTPC
i
SARS-CoV-2 AGER
ii
D
AB-PAS
Vessel
Large airway
i
MUC5B
ii
MUC5B
MUC5AC
v
iv
iii
MUC5B
MUC5AC
Lumen
SMG
iv
MUC5B
MUC5AC
v

A

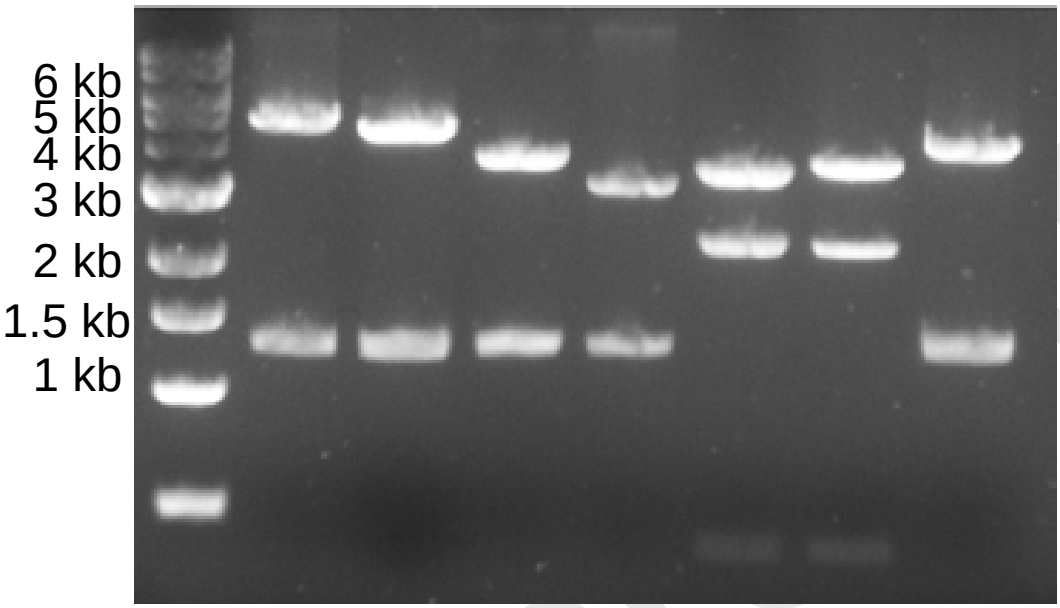
A
B
C
D
E
F
G
6 kb
5 kb
4 kb
3 kb
2 kb
1.5 kb
1 kb

B

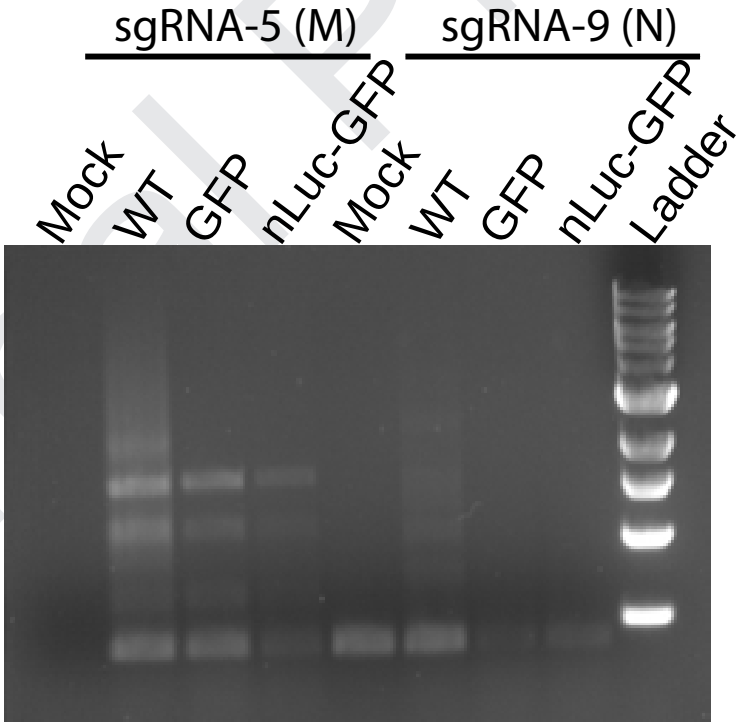
sgRNA-5 (M)
sgRNA-9 (N)
Mock
WT
GFP
nLuc-GFP
Mock
WT
GFP
nLuc-GFP
Ladder

C

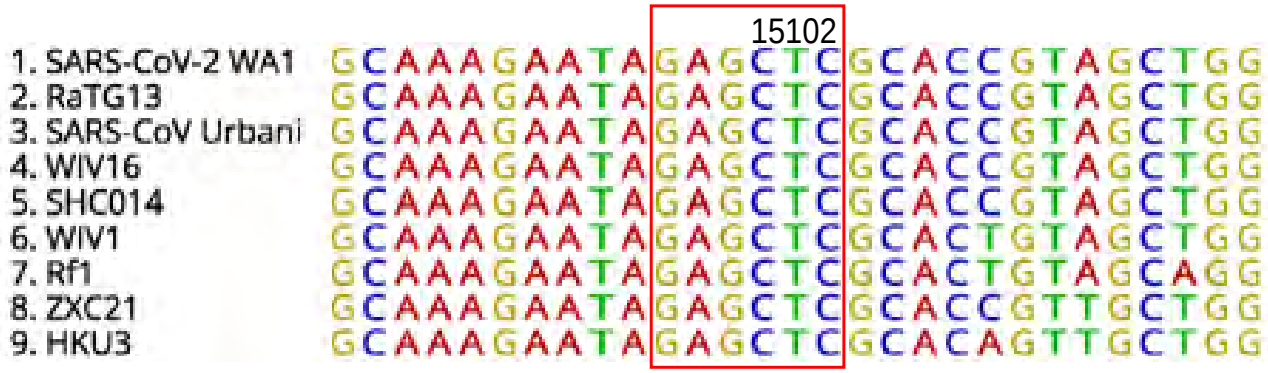
SacI
15102
1. SARS-CoV-2 WA1 GCAAAAGAATAGAGCTCGCACCGTAGCTGG
2. RaTG13 GCAAAAGAATAGAGCTCGCACCGTAGCTGG
3. SARS-CoV Urbani GCAAAAGAATAGAGCTCGCACCGTAGCTGG
4. WIV16 GCAAAAGAATAGAGCTCGCACCGTAGCTGG
5. SHC014 GCAAAAGAATAGAGCTCGCACCGTAGCTGG
6. WIV1 GCAAAAGAATAGAGCTCGCACTGTAGCTGG
7. Rf1 GCAAAAGAATAGAGCTCGCACTGTAGCAGG
8. ZXC21 GCAAAAGAATAGAGCTCGCACCGTTGCTGG
9. HKU3 GCAAAAGAATAGAGCTCGCACAGTTGCTGG

A

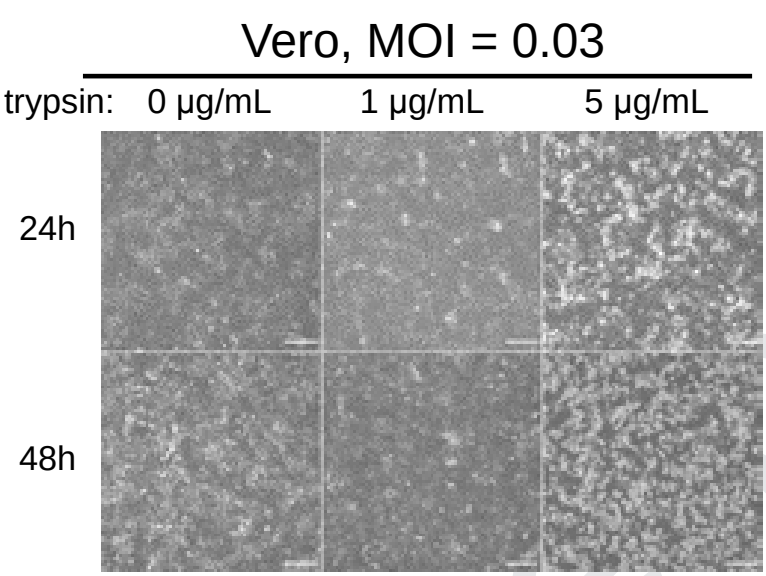

B

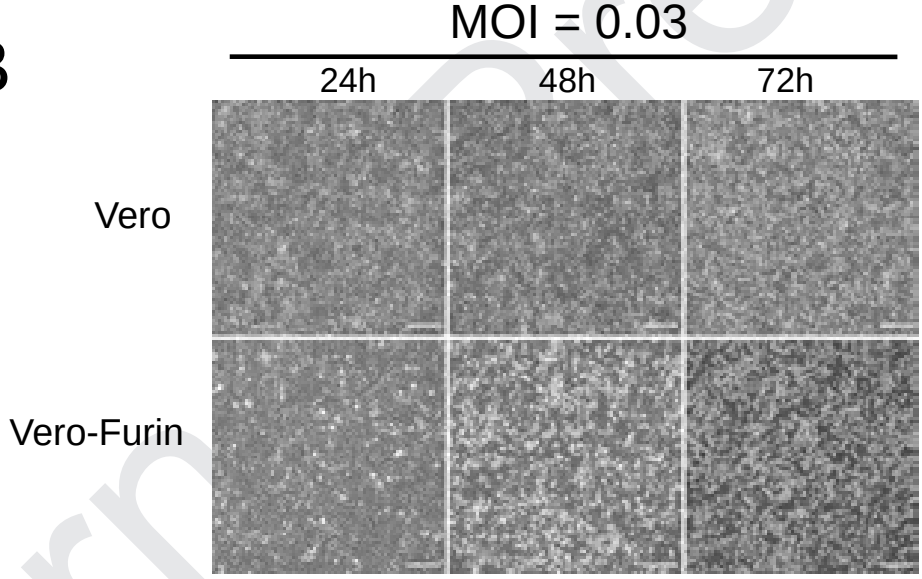

C

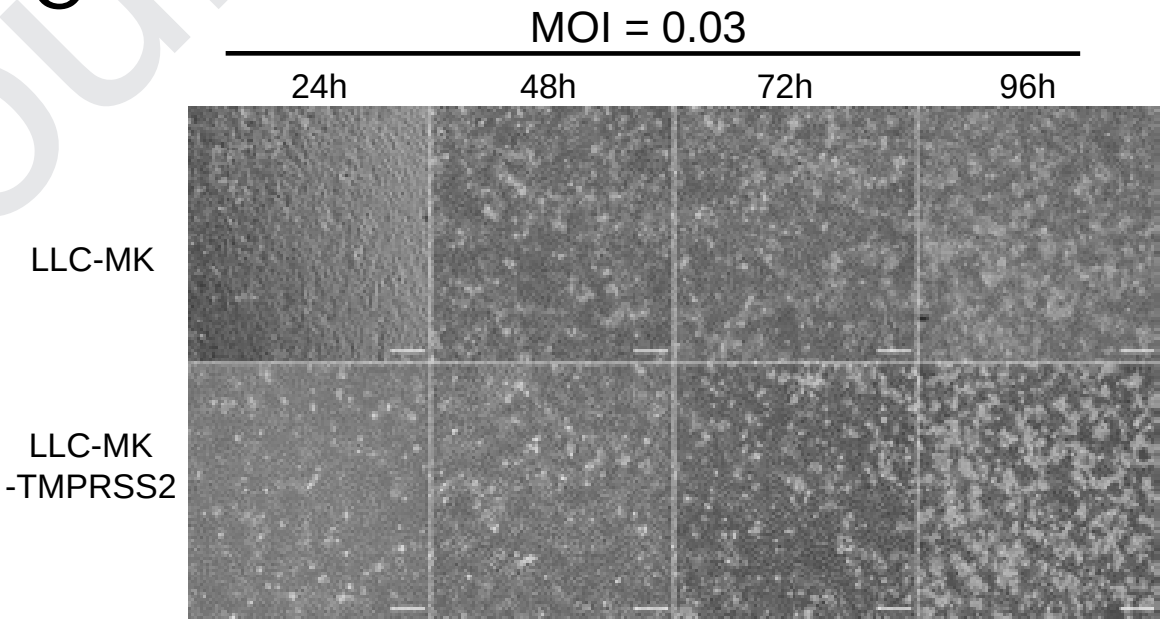

A

Tonsil

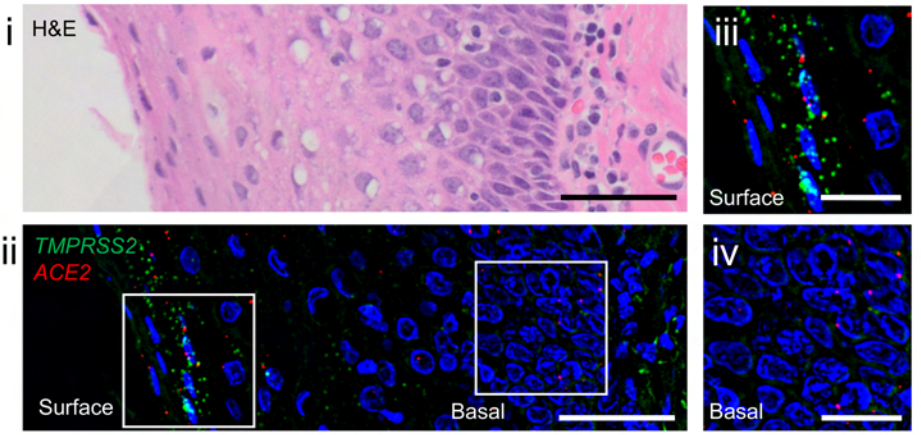

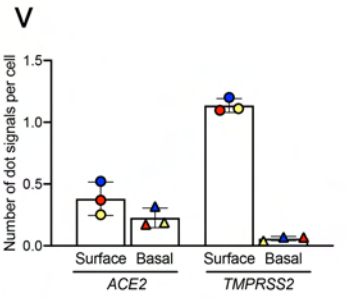

B

Nasal surface epithelium

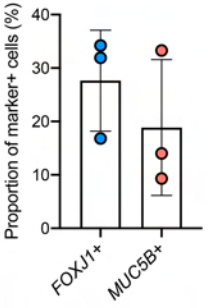

C

Nasal submucosal gland

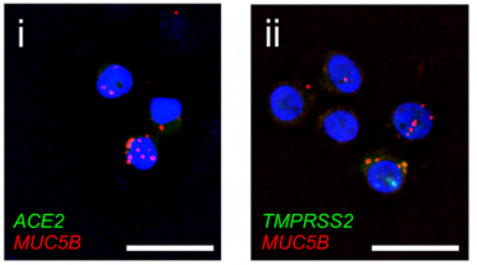

iii

Among 200 *MUC5B*-positive cells	
ACE2-positive	1
ACE2-negative	199

Among 200 *MUC5B*-positive cells	
TMPRSS2-positive	16
TMPRSS2-negative	184

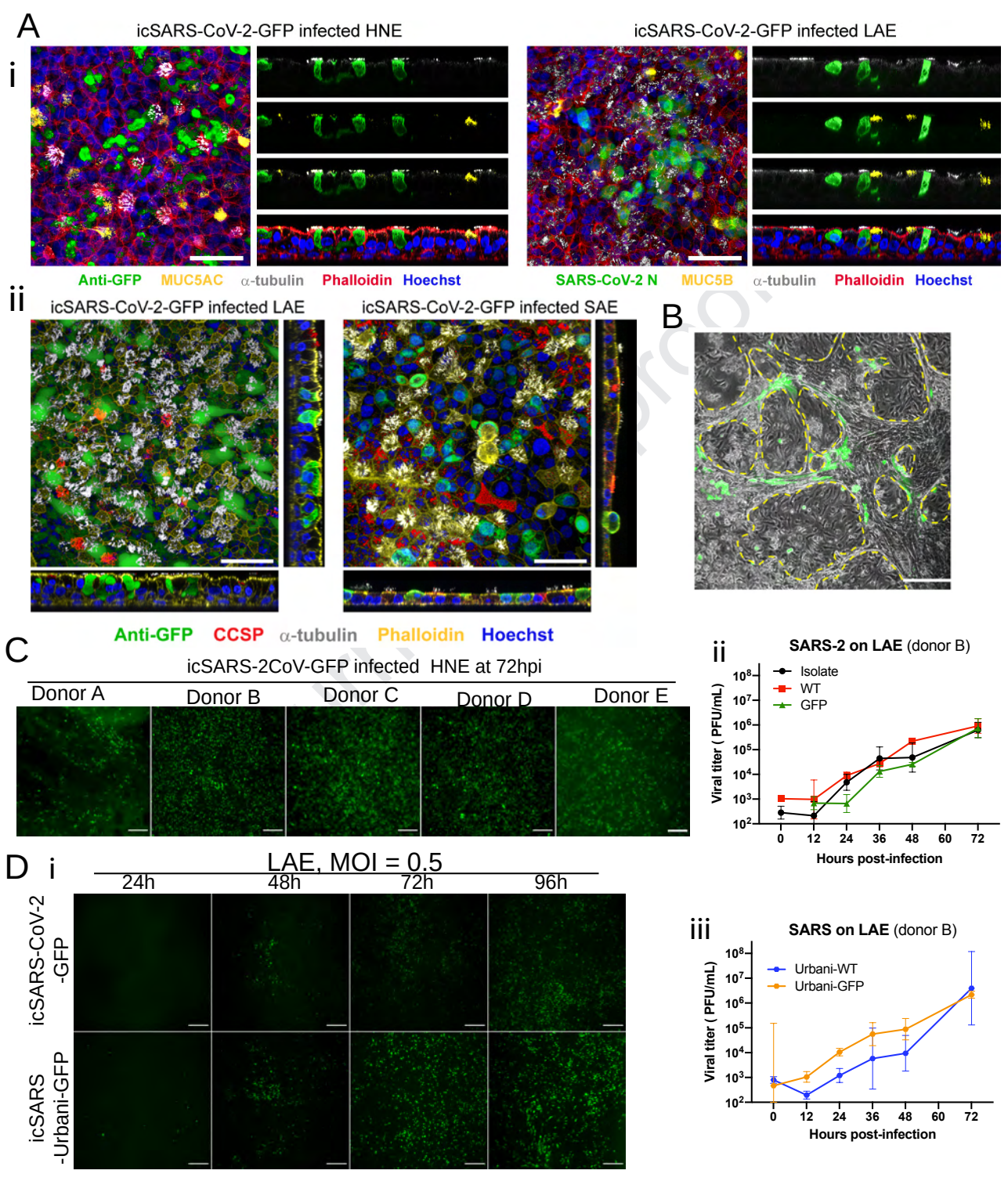
A
i
icSARS-CoV-2-GFP infected HNE
icSARS-CoV-2-GFP infected LAE
Anti-GFP MUC5AC α-tubulin Phalloidin Hoechst
SARS-CoV-2 N MUC5B α-tubulin Phalloidin Hoechst
ii
icSARS-CoV-2-GFP infected LAE
icSARS-CoV-2-GFP infected SAE
B
Anti-GFP CCSP α-tubulin Phalloidin Hoechst
C
icSARS-2CoV-GFP infected HNE at 72hpi
Donor A
Donor B
Donor C
Donor D
Donor E
ii
SARS-2 on LAE (donor B)
Isolate
WT
GFP
Viral titer (PFU/mL)
Hours post-infection
D i
LAE, MOI = 0.5
24h
48h
72h
96h
icSARS-CoV-2 -GFP
icSARS -Urbani-GFP
iii
SARS on LAE (donor B)
Urbani-WT
Urbani-GFP
Viral titer (PFU/mL)
Hours post-infection

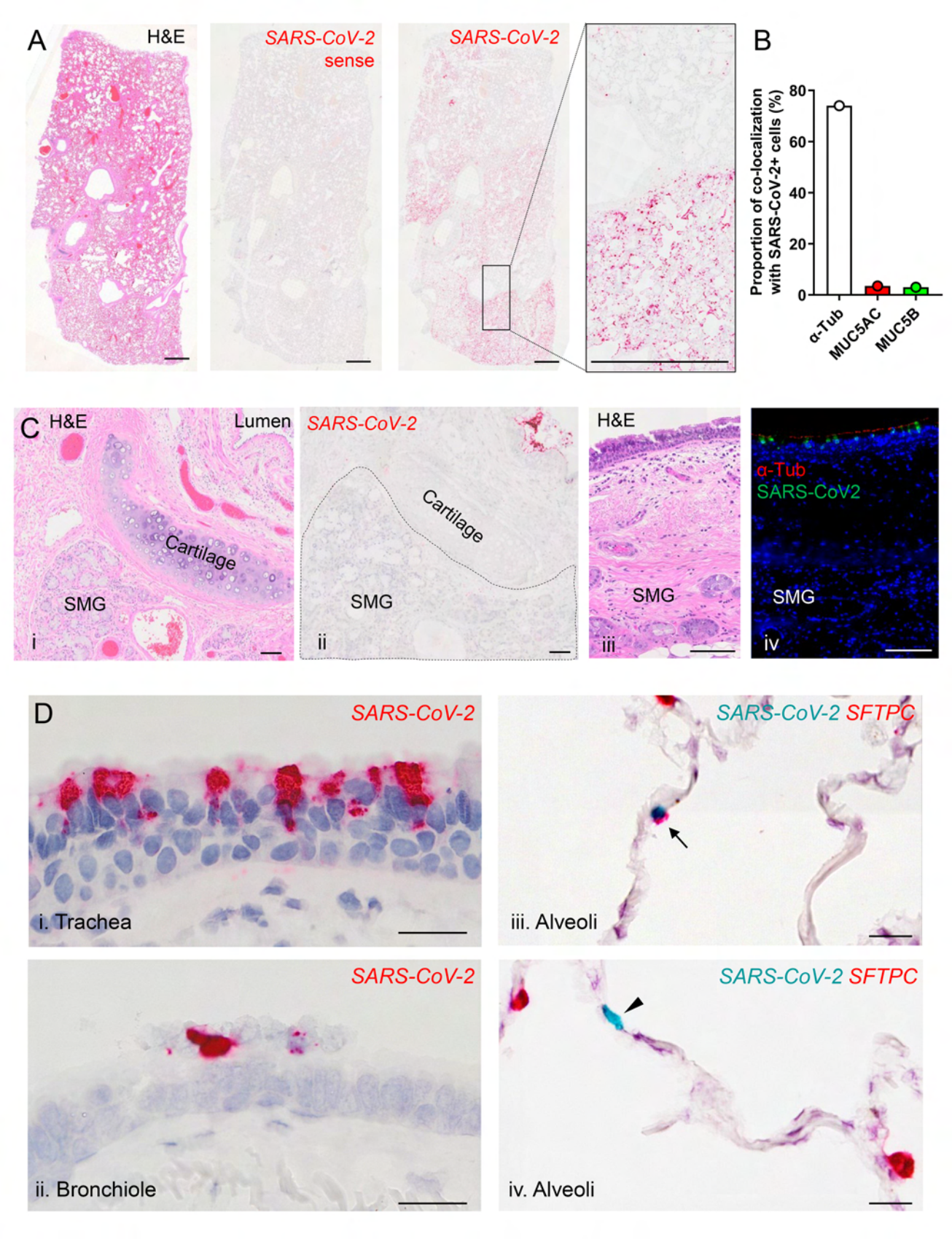
A
H&E
SARS-CoV-2 sense
SARS-CoV-2
B
Proportion of co-localization with SARS-CoV-2+ cells (%)
80
60
40
20
0
α-Tub
MUC5AC
MUC5B
C
H&E
Lumen
Cartilage
SMG
i
SARS-CoV-2
Cartilage
SMG
ii
H&E
SMG
iii
α-Tub
SARS-CoV2
SMG
iv
D
SARS-CoV-2
i. Trachea
SARS-CoV-2 SFTPC
iii. Alveoli
SARS-CoV-2
ii. Bronchiole
SARS-CoV-2 SFTPC
iv. Alveoli

Table S1. Demographics of normal subjects studied and experimental use, Related to the STAR Methods

#	Age	Sex	Smoking History	Airway region	Collection	Related figure
1	40	M	NS	Bronchi	Bronchial brushing	Fig. 4E-I
2	22	M	NS	Bronchi	Bronchial brushing	Fig. 4E-I
3	25	M	NS	Bronchi	Bronchial brushing	Fig. 4E-I
4	48	M	Unknown	Nose	Excess surgical tissue	Fig. 4A
5	58	M	Unknown	Nose	Excess surgical tissue	Fig. 4A
6	57	M	Unknown	Nose	Excess surgical tissue	Fig. 4E-I
7	41	F	Unknown	Nose	Excess surgical tissue	Fig. 4E-I
8	73	F	Unknown	Nose	Excess surgical tissue	Fig. 4E-I
9	15	M	NS	Lung	Transplant donor lung	Fig. 4Evi, 4Evii
10	25	M	NS	Lung	Transplant donor lung	Fig. 4Evi, 4Evii
11	19	M	NS	Lung	Transplant donor lung	Fig. 4Evi, 4Evii
12	17	F	NS	Lung	Transplant donor lung	Fig. 4A, 5A
13	52	F	NS	Lung	Transplant donor lung	Fig. 4A, 5A
14	37	M	NS	Lung	Transplant donor lung	Fig. 4A, 5A
15	44	M	NS	Lung	Transplant donor lung	Fig. 4A, 5A
16	55	F	NS	Lung	Transplant donor lung	Fig. 4A, 4C, 5A
17	27	M	NS	Lung	Transplant donor lung	Fig. 4A, 5A
18	35	F	5 cigarettes/ month	Nose/ Bronchi	Nasal scrape/ Bronchial brushing	Fig. 4B
19	22	M	NS	Nose/ Bronchi	Nasal scrape/ Bronchial brushing	Fig. 4B
20	39	F	NS	Nose/ Bronchi	Nasal scrape/ Bronchial brushing	Fig. 4B
21	35	M	5 PY	Nose/ Bronchi	Nasal scrape/ Bronchial brushing	Fig. 4B
22	23	M	NS	Nose/ Bronchi	Nasal scrape/ Bronchial brushing	Fig. 4B
23	22	F	NS	Nose/ Bronchi	Nasal scrape/ Bronchial brushing	Fig. 4B
24	22	F	NS	Nose/ Bronchi	Nasal scrape/ Bronchial brushing	Fig. 4B
25	42	M	NS	Nose/ Bronchi	Nasal scrape/ Bronchial brushing	Fig. 4B
26	35	F	NS	Lung	Transplant donor lung	Fig. 4C
27	53	F	NS	Lung	Transplant donor lung	Fig. 4C
28	24	M	NS	Lung	Transplant donor lung	Fig. 4C
29	25	M	NS	Lung	Transplant donor lung	Fig. 4C
30	15	M	NS	Lung	Transplant donor lung	Fig. 4C
31	27	M	NS	Lung	Transplant donor lung	Fig. 4C
32	39	F	Unknown	Tonsil	Excess surgical tissue	Fig. S3
33	37	F	Unknown	Tonsil	Excess surgical tissue	Fig. S3
34	38	F	Unknown	Tonsil	Excess surgical tissue	Fig. S3

NS = never smoker, PY = pack-year

Table S2. Demographics of CF subjects studied for RNA-ISH experiment, Related to the STAR Methods

#	Age	Sex	CFTR mutation	Airway region	Collection	Related figure
1	45	F	DF508/N1303K	Lung	Lung transplantation	Fig. 5A
2	42	F	DF508/DF508	Lung	Lung transplantation	Fig. 5A
3	30	F	DF508/DF508	Lung	Lung transplantation	Fig. 5A
4	15	M	DF508/W1282X	Lung	Lung transplantation	Fig. 5A
5	34	M	DF508/W1282X	Lung	Lung transplantation	Fig. 5A
6	59	F	DF508/N1303K	Lung	Lung transplantation	Fig. 5A